

Phase dynamics of effective drag and lift in vortex-induced vibration at low mass–damping

E. Konstantinidis^{1†} J. Zhao² D. Lo Jacono³ J. Leontini⁴ and J. Sheridan²

¹Department of Mechanical Engineering, University of Western Macedonia, Kozani, 50132, Greece

²Department of Mechanical and Aerospace Engineering, Monash University, Melbourne, VIC 3800, Australia

³Institut de Mcanique des Fluides de Toulouse (IMFT) CNRS, UPS, Universit de Toulouse, Alle Camille Soula, F-31400 Toulouse, France

⁴Department of Mechanical Engineering and Product Design Engineering, Swinburne University of Technology, John St Hawthorn, 3162, Australia

In this work, we investigate the dynamics of vortex-induced vibration of an elastically mounted cylinder with very low values of mass and damping by employing a decomposition of the total hydrodynamic force into drag and lift components that act along and normal to, respectively, the instantaneous effective angle of attack as the cylinder oscillates transversely to the uniform free stream. Initially, we consider the hydro-elastic cylinder as a non-linear dynamical system and focus on the phase dynamics between fluid forcing and cylinder motion in the synchronization range, which comprises three distinct branches of response, the initial, upper and lower. When we examine time series of the phase difference between the transverse fluid force and the cylinder displacement we observe repeated phase slips separating periods of constant phase or continuous drifting of the phase difference at some reduced velocities in the second half of the upper branch. Such features illustrate a paradoxical loss of phase locking between the driving force and the response about the middle of the synchronization range. However, when we examine time series of the phase difference between the lift component and the cylinder displacement, we observe strong phase locking throughout the synchronization range, while the mean phase difference varies linearly with the common frequency of lift and displacement. Moreover, the mean lift phase increases linearly as a function of the reduced velocity in the upper branch but remains nearly constant in the lower branch, which elucidates the different dynamics in each response branch. The transition between the upper and lower branches is marked by distinct changes in both lift frequency and phasing. The indirect measurements confirm that the drag component acts as a damping factor opposing the cylinder oscillation velocity whereas the lift component provides the necessary fluid excitation for free vibration to be sustained as expected from theoretical considerations. Remarkably, the lift magnitude scales linearly with the same combined parameter as the equation of motion requires for the transverse force in-phase with the cylinder velocity. A simple model for the drag and lift components is introduced which can satisfactorily describe their damping and excitation function in vortex-induced vibration. We employ the model to explain (a) the cause of chaotic response in the second half of the upper branch and (b) the constancy of the response frequency in the lower branch, i.e. the origin of classical lock-in. Both phenomena are shown to be related to incompatible requirements imposed on the phasing of the lift component by the hydrodynamics of the unsteady wake flow and the dynamics of the cylinder free motion. Finally, we demonstrate

† Email address for correspondence: ekonstantinidis@uowm.gr

that the transition between the upper and lower branches comprises bistable dynamics where two stable states exist over different periods of time at constant reduced velocity. In each stable state, the phasing of the lift with respect to displacement is different, which further illustrates the utility of the proposed force decomposition.

Key words: flow-structure interaction, unsteady hydrodynamics, phase dynamics

1. Introduction

Vortex-induced vibration (VIV) has been the subject of extensive research over the past six decades because of its importance in engineering applications, such as riser pipes transporting oil from sea bottom, supporting cables and pylons of offshore platforms, on one hand and because of the complexity of the fluid-mechanical phenomena on the other hand. There are several review papers on the subject including Parkinson (1971), King (1977), Griffin (1981), Bearman (1984), Sarpkaya (2004), Williamson & Govardhan (2004), Gabbai & Benaroya (2005) and Bearman (2011). Much of the fundamental research has dealt with rigid circular cylinders elastically mounted so as to have one degree of freedom to oscillate transversely to a uniform free stream. This can be considered as the simplest configuration to study VIV and the building block to understand phenomena in more complex configurations (Williamson & Govardhan 2004). Yet, semi-empirical codes and guidelines used in the industry also rely on databases of the hydrodynamic forces on rigid cylinders undergoing single degree-of-freedom transverse oscillations. The equation of motion for a freely-vibrating hydro-elastic cylinder can be written as

$$m (\ddot{y} + 2\pi f_n \zeta \dot{y} + 4\pi^2 f_n^2 y) = F_y, \quad (1.1)$$

where y is the displacement of the cylinder and each overdot represents a derivative with respect to time, m is the mass of the oscillating structure, f_n is the natural frequency of the structure, ζ is the damping ratio, and F_y is the time-varying hydrodynamic force acting in the direction of motion. In the above form, the left-hand side of the equation of motion is a second-order differential equation that comprises parameters exclusively associated with the solid structure. Thus, the structural dynamics is linear and any non-linearity is introduced by the hydrodynamic forcing term on the right-hand side. As a consequence, the modelling of the hydrodynamic force F_y has significant ramifications for understanding VIV, the main theme of the present work.

In experimental studies, the natural frequency and the damping ratio are typically determined from free-decay tests in still fluid (Blevins 2001). Measured values from free-decay oscillations in still fluid differ from the true values, which correspond to the solid structure in vacuum (Sarpkaya 2004). Blevins (2009) has provided a hydrodynamic model for oscillations of a cylinder in still fluid that can be used to estimate the true values from free-decay oscillations in still fluid. For tests in air, which has density much lower than the average density of solid structures, measured values from free-decay oscillations can be regarded to a good approximation as the true values. For tests in water or fluids with a density comparable to the average density of the structure, the surrounding fluid alters the measured natural frequency and damping ratio. In numerical simulations, the true structural damping and mass in vacuum are exclusively set as input parameters (see, e.g., Lucor *et al.* 2005; Leontini *et al.* 2006a).

On the theoretical side, much of our understanding of VIV relies on the approximation

of pure harmonic oscillation (Bearman 1984, 2011). That is, assuming that the displacement of the cylinder can be described as a sinusoidal function of time t ,

$$y(t) = A \sin(2\pi ft), \quad (1.2)$$

where A and f respectively are the amplitude and the frequency of oscillation. By taking the first and second order derivatives of (1.2) and inserting into (1.1), it follows directly that the hydrodynamic force F_y is also a pure harmonic function of time, which is typically expressed in terms of its magnitude C_y and its phase lag ϕ as

$$F_y(t) = \frac{1}{2}\rho U_\infty^2 D L C_y \sin(2\pi ft + \phi), \quad (1.3)$$

where ρ is the density of the fluid, U_∞ is the velocity of the free stream, D is the outer diameter of the cylinder, and L is the (immersed) length of the cylinder. In the following, it is assumed that the hydrodynamic force and the oscillation are homogeneous along the spanwise direction so that it is permissible to consider a unit length of the cylinder. Note that if the motion is harmonic, it is not necessary to assume that the displacement $y(t)$ and the force $F_y(t)$ be synchronous; this follows directly from the equation of motion (1.1). Nonetheless, the equation of motion is in itself a simplistic model of the structural dynamics and minor deviations from the ideal behaviour might be anticipated in practice.

By replacing the assumed harmonic motion (1.2) and hydrodynamic force (1.3) in the equation of motion (1.1) and equating the factors of the sine and cosine terms on both sides, a set of two algebraic equations is obtained. Khalak & Williamson (1999), among other investigators, solved the set of equations for the response amplitude and frequency and obtained the following relationships:

$$A^* = \frac{C_y \sin \phi}{4\pi^3 (m^* + C_A) \zeta} \left(\frac{U^*}{f^*} \right)^2 f^*, \quad (1.4)$$

$$f^* = \sqrt{\frac{m^* + C_A}{m^* + C_{EA}}}, \quad (1.5)$$

where C_{EA} is an ‘effective added mass coefficient’ that depends on the component of the hydrodynamic force in-phase with the cylinder displacement:

$$C_{EA} = \frac{C_y \cos \phi}{2\pi^3 A^*} \left(\frac{U^*}{f^*} \right)^2. \quad (1.6)$$

In the above equations that have been written in dimensionless form, $A^* = A/D$, $f^* = f/f_{n,\text{fluid}}$, $m^* = 4m/\pi\rho DL$, and $U^* = U_\infty/f_{n,\text{fluid}}D$, where $f_{n,\text{fluid}}$ is the natural frequency measured in still fluid. The added mass coefficient C_A for small amplitude oscillations in otherwise still fluid takes a value of 1.0 (Williamson & Govardhan 2004). The above set of equations shows that the normalized amplitude and frequency of response depends on the mass ratio m^* , the damping ratio ζ , and the reduced velocity U^* . These dependencies have been relatively well established from experimental observations where U^* is typically varied over the range of interest. For hydro-elastic cylinders with very low mass and damping so that the product $m^*\zeta$ is of the order of 0.01 or less, Khalak & Williamson (1996, 1999) identified four distinct branches of response with changing U^* : the initial excitation region, the upper branch of very high amplitude, the lower branch of moderate amplitude, and the desynchronization region. Transitions between response branches involve jumps in the cylinder oscillation amplitude and are accompanied by changes in the mode of vortex shedding (Govardhan & Williamson 2000). For hydro-elastic systems with high values of combined massdamping, the upper branch of very

high response amplitude does not appear as found in early experiments by Feng (1968) and more recently by Klamo *et al.* (2006). A very recent study showed that the upper branch does not disappear at high levels of damping but jumps in response amplitude become smeared out instead; the upper branch still exists as can be inferred from the variation of the response frequency (Soti *et al.* 2018). Both upper and lower branches have been associated to synchronization, i.e. the oscillation and the fluid forcing synchronize at a common frequency. However, the common frequency increases in the upper branch but remains fairly constant in the lower branch, which indicates that the dynamics is different in these two branches.

Lock-in is the phenomenon where the frequency of vortex shedding becomes self-tuned to approximately the natural frequency of the hydro-elastic cylinder for a range of free-stream velocities. It should be noted that we define ‘lock-in’ in a manner that is not tantamount to ‘synchronization’ (see also Konstantinidis 2014). Since the classical work of Feng (1968) the phenomenon was considered to be the result of the structural motion dominating the vortex formation process thereby controlling the frequency at which vortices are shed in the wake. Govardhan & Williamson (2000) showed that classical lock-in is observed in the lower branch. They showed that the lock-in frequency depends on the mass ratio according to the following formula,

$$f_{\text{lower}}^* = \sqrt{\frac{m^* + 1}{m^* - 0.54}}, \quad (1.7)$$

obtained from an empirical fit to experimental data with different mass ratios for very low values of $m^*\zeta$. The recent measurements of Soti *et al.* (2018) showed that the frequency of cylinder response is constant in the lower branch also at high levels of damping. On the other hand, Gharib (1999) did not observe lock-in behaviour in his experiments for mass ratios below 10. Experimental tests by Blevins & Coughran (2009) showed that lock-in tendency weakens with increasing either mass or damping of the hydro-elastic cylinder. A lock-in region of fairly constant frequency of cylinder response is also not evident in the experiments of Lee & Bernitsas (2011), who conducted extensive tests with variable levels of damping and stiffness, which were adjusted by a virtual damper-spring apparatus.

The force coefficients in-phase with cylinder displacement $C_y \cos \phi$ and velocity $C_y \sin \phi$, which appear in the solution of the linearised problem, depend on the motion of the cylinder in a highly complex manner. Sarpkaya (2004) noted that all non-linearity in the fluid dynamics has to be embodied in just two parameters: the magnitude C_y and phase ϕ of the fluid force. A line of thought is to derive the force coefficients from measurements using controlled harmonic oscillations (see, e.g., Gopalkrishnan 1993; Morse & Williamson 2009*a*). The force coefficients are typically taken as Fourier averages over many cycles of oscillation of the transverse component of the unsteady force acting on the cylinder. Then, it is possible in principle to predict the free response of an elastically mounted cylinder using the fluid forcing database. Morse & Williamson (2009*b*) found that matching the Reynolds number between controlled and free vibrations is important for successfully predicting the peak oscillation amplitude in the upper branch. Blevins (2009) adopted the converse approach: he computed the force coefficients from the harmonic model equations for free oscillations of a cylinder transverse to a free stream; both steady and transient conditions were employed to cover a parameter space of normalized amplitude and frequency of interest. Then, he employed the constructed force database to predict the response for systems with different levels of structural damping.

The component of the fluid force in-phase with the cylinder velocity $C_y \sin \phi$, often referred as the excitation coefficient, can sustain self-excited oscillations if it is positive, a

requirement that stems directly from (1.4). In the special case of zero structural damping ($\zeta = 0$), which is often employed in numerical simulations, $C_y \sin \phi$ has to be zero. The excitation coefficient $C_y \sin \phi$ also represents the normalized energy transfer from the fluid to the cylinder motion over an average cycle (Morse & Williamson 2009b). Several investigators employed controlled harmonic motion to identify the regions of positive energy transfer where free vibration is possible (Tanida *et al.* 1973; Hover *et al.* 1998; Carberry *et al.* 2005). As shown by Morse & Williamson (2009b, 2010), a very large number of tests is necessary in order to precisely map the regions of positive energy transfer in the parameter space of normalized amplitude and wavelength $\{A^* : U^*/f^*\}$ and replicate the dynamics of free vibration in different response branches. The latter investigators further noted that an additional requirement for free vibration is the stability of the equilibrium solutions.

There is some debate whether the assumption of harmonic motion is a good approximation of VIV under all circumstances. Sarpkaya (2004) discussed possible limitations of this linearised approach when the oscillations have amplitude and/or frequency modulations. Marzouk (2011) carried out numerical simulations at low Reynolds numbers and found that a constructed forced vibration that does not contain the third-superharmonic component of the main oscillation frequency failed to reproduce some details of the fluid force although the magnitude of this component is about 400-fold less than the magnitude of the fundamental component. This was significant at low values of damping and became less significant at high damping values for a hydro-elastic cylinder with a mass ratio of unity. Konstantinidis (2017) noted, by examining data from both controlled and free vibrations at a Reynolds number of 100 from numerical simulations of other investigators, that VIV has to deviate from pure harmonic since some operating points of free oscillation for a system without damping do not fall atop the contour of zero energy transfer in the parameter space of normalized amplitude and frequency. Zhao *et al.* (2014a) accurately measured the free vibration of a hydro-elastic cylinder and used the recorded displacement signal to drive a cylinder in controlled motion replicating the free vibration; they found that the controlled motion did not exactly replicate the same flow patterns and the same phasing of the hydrodynamic force observed in free vibration at a point near peak oscillation amplitude in the upper branch.

The accurate measurement of the phase lag ϕ between fluid force $F_y(t)$ and displacement $y(t)$ is critical for analysing and interpreting fluid forcing data. This is so because the phase of the fluid force is generally considered to be influenced by the character or mode of vortex shedding (Gabbai & Benaroya 2005; Bearman 2009). For controlled harmonic oscillation of a cylinder transversely to a free stream, Morse & Williamson (2009a) have provided high-resolution contours of ϕ in the parameter space of normalized amplitude and wavelength $\{A^* : U^*/f^*\}$. They showed that contours are not continuous across the entire parameter space but distinct boundaries appear where changes in the regime of vortex shedding were identified by flow visualization. However, the relationship between fluid force phase and vortex shedding mode remains rather unclear due to the lack of an analytical model that can explain physically and quantitatively the variations in ϕ within each regime. In free vibration, variations in the phase of the fluid force are even more difficult to interpret due to restrictions posed by the equation of the cylinder free motion. Assuming that free vibration is pure harmonic, Sarpkaya (2004) derived the following relationship :

$$\tan \phi = \frac{2\zeta f f_n}{f_n^2 - f^2}. \quad (1.8)$$

As a consequence, ϕ must change sign at $f = f_n$, which brings in an extra dependency

on the mechanical properties of hydro-elastic cylinder in addition to the dependency on the amplitude and frequency of cylinder motion. Equation (1.8) shows that ϕ is only a function of the damping ratio ζ and the frequency ratio f/f_n irrespectively of the mass ratio m^* and the reduced velocity U^* . At very low levels of damping ζ of the order of 10^{-3} in particular, ϕ is constrained to values close to 0° or 180° and a phase shift by approximately 180° occurs at $f = f_n$. With such a limited range of permissible ϕ values, it becomes hard to unambiguously discern changes in the mode of vortex shedding.

The phase lag between force and displacement can also change during a test at some fixed reduced velocity. By employing the Hilbert transform to compute the instantaneous phase during free vibration, Khalak & Williamson (1997) showed that for operating points in the transition region from the upper branch to the lower branch intermittent switching of the instantaneous phase between 0° and 180° occurs. Their finding highlights that the use of the mean phase may be less accurate or less representative in the transition region, at least. More recently, Zhao *et al.* (2014a) also employed the Hilbert transform to link the phase dynamics and the vortex dynamics in the wake of a freely-vibrating cylinder. They confirmed that the upper \leftrightarrow lower branch transition is associated with intermittent switching of the instantaneous phase. Although it was clear that different vortex patterns or wake modes occurred during a test, the relationship to intermittent switching in the phase of the unsteady force with respect to the displacement may require further investigation. A pertinent question is if the wake can almost instantly switch between different modes since this process may require several cycles of oscillation to complete. Phase switching appears to be more sudden than would be physically required for vortex shedding to switch from one side to the other side of an oscillating cylinder as a 180° jump in phase implies. Furthermore, Zhao *et al.* (2014a) found evidence of chaos due to mode competition near the middle of the upper branch where the wake switches between at least two distinct modes. One of the objectives of the present study is to examine the origin of phenomenologically chaotic dynamics observed in the upper branch.

In this study, we approach VIV using an alternative perspective. As a cylinder oscillates transversely to a free stream, the effective angle of attack changes. The relative velocity between the free-stream velocity U_∞ and the cylinder velocity \dot{y} is $\mathbf{U} = U_\infty \mathbf{i} - \dot{y} \mathbf{j}$, where \mathbf{i} and \mathbf{j} respectively are the unit vectors in the streamwise x and transverse y directions. Here, we consider the kinematically analogous case where the cylinder is towed through still fluid with its axis maintained perpendicular to the direction of motion (Konstantinidis 2013). The cylinder moves forwards at constant speed U_∞ while its speed in the transverse direction changes. We define the ‘effective’ drag F_D and lift F_L as the components of the total hydrodynamic force F acting along the instantaneous angle of attack a_{eff} and normal to the drag direction, respectively, as shown in figure 1. In the following, drag and lift will always their effective values as per their definition in figure 1. The components of the force in the horizontal direction F_x and the vertical direction F_y are those customarily measured in the fixed frame of reference of the laboratory. The selection of a relative frame of reference has some important implications. As the cylinder is towed in a prescribed path through still fluid, it does work on the fluid at the rate $\mathbf{F} \cdot \mathbf{U}$ where \mathbf{F} and \mathbf{U} respectively are the instantaneous vectors of the hydrodynamic force and the cylinder velocity. So the fluid’s drag force resists the motion of the cylinder, i.e. it is a reactive force. Thus, the force aligned with the instantaneous velocity of the cylinder in the relative reference frame can only transfer energy from the cylinder to the fluid. This must also be true in the fixed reference frame since the two cases are kinematically equivalent. In the case of an elastically-mounted cylinder undergoing free vibration transversely to a uniform free stream, the energy required to excite and sustain

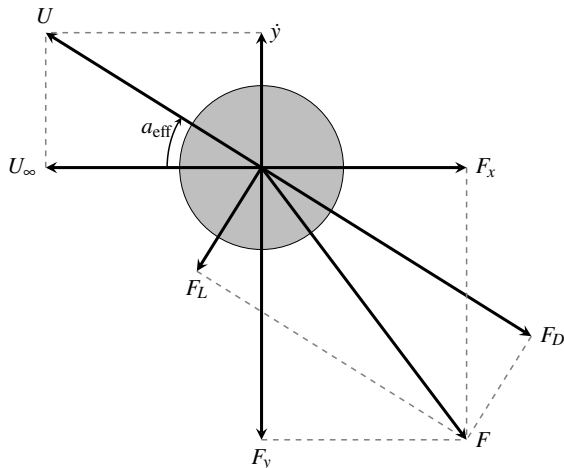


FIGURE 1. Diagram of the main vectors employed in the present study in the relative frame of reference moving with velocity U as the cylinder moves through still fluid.

the oscillations can only result from the lift component, which therefore may be directly linked to the vortex dynamics in the wake. We use this approach in an attempt to gain insight into the dynamics of VIV and answer outstanding questions posed in the foregoing paragraphs.

2. Experimental set-up

The experiments were conducted in a free-surface recirculating water channel of the FLAIR group at Monash University. Figure 2 shows a schematic of the experimental configuration. The water channel has a test section of 0.6 m (width) \times 0.8m (height) \times 4m (length) and the background turbulence level is below 1%. A rigid cylinder made of carbon fibre tubing was elastically mounted from above the free surface on low-friction air bearings. The cylinder had an outer diameter of $D = 25$ mm and an immersed length of $L = 620$ mm, giving an aspect ratio of $L/D = 24.8$. A raised platform was placed at the bottom of the water channel with a gap of approximately 1 mm to the free end of the cylinder to promote two dimensionality of the flow along the span. The ratio of the mass of the oscillating structure to the mass of the fluid displaced by the cylinder was estimated to be $m^* = 3.00$. The natural frequency of the mechanical system was measured from free-decay tests, which resulted in values of $f_{n,\text{air}} = 0.835$ Hz in still air and $f_{n,\text{water}} = 0.717$ Hz in still water. The ratio of the mechanical damping to the critical damping of the mechanical oscillator was estimated from the free-decay tests in air to be 3.5×10^{-3} . In this study, it is assumed that the mechanical properties measured in still air approximately correspond to the properties of the system in vacuum. The free-stream velocity was increased from 43.1 to 260.4 mm/s at 96 different values leaving sufficient time between measurements for conditions to settle. The adjustment of the free-stream velocity resulted in variations in the reduced velocity, defined as $U^* = U_\infty/f_{n,\text{water}}D$, between 2.4 and 14.5 corresponding to Reynolds numbers in the range from 1250 to 7550. It should be noted that in the presentation of the results we employ the reduced velocity based on the natural frequency of the structure in still water for consistency with previous studies.

The displacement of the oscillating cylinder was monitored using a non-contact magne-

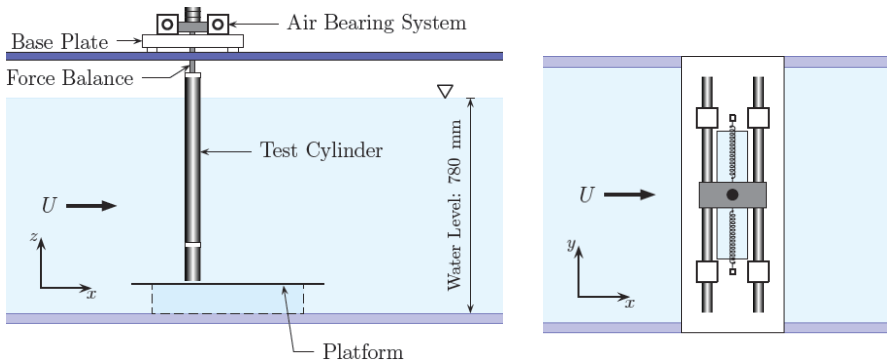


FIGURE 2. Schematic of the experimental facility.

tostrictive linear variable differential transformer having an accuracy within 0.01% of the 250 mm full-scale range, giving a displacement measurement precision of approximately $0.001D$. The streamwise and transverse components of the fluid force acting on the oscillating cylinder were simultaneously measured using a two-component force balance having a resolution of 0.005 N. The measurement of the force was based on strain gauges configured in a full Wheatstone bridge circuit. For the transverse component, the inertial force due to the cylinders acceleration was subtracted to recover the instantaneous fluid force. Time series of the displacement, $y(t)$, streamwise, $F_x(t)$, and transverse, $F_y(t)$, components were collected over 300 s at a sampling rate of 100 Hz yielding 3×10^4 samples per channel.

Details about the experimental set-up and measurement techniques can also be found in Nemes *et al.* (2012) and Zhao *et al.* (2014*a,b*). A detailed comparison of response characteristics of rigid cylinders undergoing VIV obtained with the experimental facility used in this study, but with a different set of measurement instruments, against previous experiments from the published literature has been given in Zhao *et al.* (2014*b*) and Soti *et al.* (2018). Overall, a good match has been found in terms of both amplitude and frequency variation with reduced velocity, which provides validation for the experimental set-up employed in the present study.

3. Data processing

The components of the hydrodynamic force along and normal to the free-stream direction, F_x and F_y respectively, were measured with the force balance. The drag, F_D , and the lift, F_L , components of the total force were obtained by a transformation from the laboratory (fixed) frame of reference to one attached to the cylinder as it would move with the same relative velocity through still fluid, using the following formulas

$$F_D = F_x \cos a_{\text{eff}} - F_y \sin a_{\text{eff}}, \quad (3.1)$$

$$F_L = F_x \sin a_{\text{eff}} + F_y \cos a_{\text{eff}}, \quad (3.2)$$

where $a_{\text{eff}} = \tan^{-1}(\dot{y}/U_\infty)$ defines the instantaneous effective angle of the relative velocity vector (see figure 1). The instantaneous velocity of the cylinder was computed by numerical differentiation of the time series of the displacement, $\dot{y}(t) = dy/dt$. The signal from the displacement sensor was first low-pass filtered to avoid propagation of errors due to measurement noise in the computed velocities.

The time series of directly and indirectly measured signals were further processed to obtain their instantaneous attributes using the Hilbert transform as follows. Taking

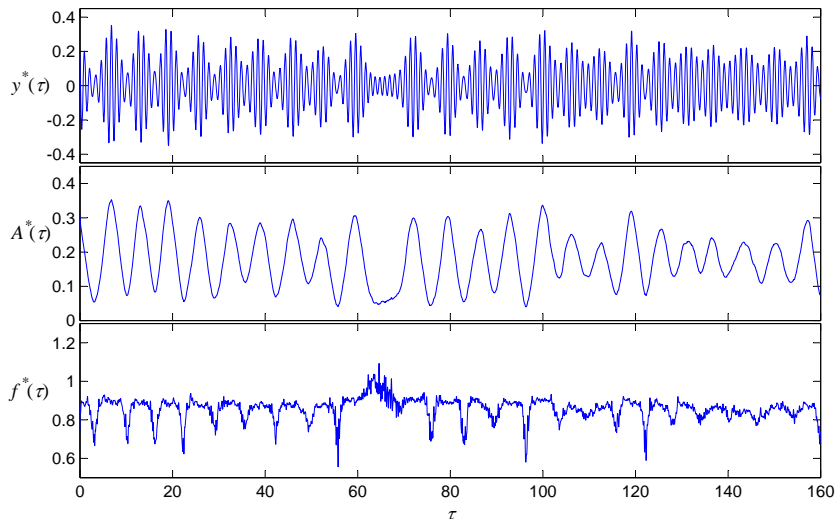


FIGURE 3. Time series of the displacement, $y^*(\tau)$, its instantaneous amplitude, $A^*(\tau)$, and its instantaneous frequency, $f^*(\tau)$, obtained from the Hilbert transform at a reduced velocity of $U^* = 4.2$. Asterisks denote normalization using the cylinder diameter and the natural frequency in still water.

an arbitrary signal $s(t)$ and its Hilbert transform $\hat{s}(t)$, the signal can be represented analytically as (Cohen 1995)

$$s_A(t) = s(t) + i\hat{s}(t) = A_s(t)e^{i\phi_s(t)}, \quad (3.3)$$

where

$$A_s(t) = \sqrt{s^2(t) + \hat{s}^2(t)} \quad \text{and} \quad \phi_s(t) = \arctan\left(\frac{\hat{s}(t)}{s(t)}\right). \quad (3.3a, b)$$

In principle, $A_s(t)$ is the instantaneous amplitude and $\phi_s(t)$ is the instantaneous phase of the signal. Then, the instantaneous ‘monocomponent’ frequency of the signal can be obtained as

$$f_s(t) = \frac{1}{2\pi} \frac{d\phi_s}{dt}. \quad (3.4)$$

Particular attention was exerted to the application of the Hilbert transform on each signal, which was padded with portions of the signal itself to decrease end effects. In addition, it is important to remove any mean component of the original signal before applying the Hilbert transform, otherwise $\hat{s}(t)$ becomes spurious; this particularly concerns the drag component of the force. Figure 3 shows how the Hilbert transform operates on the displacement signal, $y^*(\tau) = y/D$, to yield the instantaneous amplitude, $A^*(\tau) = A/D$, frequency, $f^*(\tau) = f/f_{n,\text{water}}$, where $\tau = tf_{n,\text{water}}$ is the normalized time. For the case shown at $U^* = 4.2$, the displacement signal exhibits strong modulations that cause variations of the instantaneous amplitude and phase, and thereby in the instantaneous frequency. In the presentation of the results, we clearly point out similar cases where time-averaged values of amplitude, phase, and frequency, are not fully representative of the dynamics.

The phase lag of the measured forces with respect to a reference signal (i.e. either the cylinder displacement or the relative velocity) was calculated by taking the difference of the instantaneous phases of the signal and of the reference signal, which were obtained with the Hilbert transform. For example, the instantaneous phase lag, $\phi(t)$, between the

Branch	Range	Amplitude
–	$2.4 \leq U^* < 3.2$	very low
initial	$3.2 \leq U^* < 4.7$	increasing
upper	$4.7 \leq U^* < 6.7$	high
bistable	$6.7 \leq U^* < 7.0$	intermediate
lower	$7.0 \leq U^* < 10.5$	moderate
desynchronization	$10.5 \leq U^* < 11.1$	decreasing
–	$11.1 \leq U^* \leq 14.5$	very low

TABLE 1. Response characteristics obtained from the variation of amplitude with reduced velocity.

transverse force, $F_y(t)$, and cylinder displacement, $y(t)$, is computed as $\tilde{\phi}(t) = \tilde{\phi}_{F_y}(t) - \tilde{\phi}_y(t)$, where tildes denote the instantaneous phases. Note that tildes are not used in the presentation of the results for the sake of simplicity. Generally, we wrap the instantaneous phase in the interval $[-180^\circ, 180^\circ]$ but we also employ other 360° intervals to facilitate the presentation of results. In particular, we often employ the phase interval $[-60^\circ, 300^\circ]$ in order to illustrate fluctuations of the phase about the level of 180° , which would otherwise appear as 180° jumps. Moreover, we also employ the unwrapped phase lag to better characterize phase dynamics. Results for the mean values of the phase difference are typically reported in degrees whereas instantaneous values of the phase difference (in radians) are presented in normalized form, $\phi^*(\tau) = \phi(\tau)/2\pi$.

4. Results and discussion

4.1. Direct measurements

The response of a cylinder undergoing VIV is typically characterized by the variation of the oscillation amplitude normalized by the cylinder diameter, $A^* = A/D$, and of the oscillation frequency normalized by the natural frequency in still fluid, $f^* = f/f_{n,\text{water}}$, as functions of the reduced velocity, $U^* = U/f_{n,\text{water}}D$. Here, A and f respectively denote time-averaged mean values of the instantaneous amplitude and frequency, which were computed from the Hilbert transform of the displacement signal. Figure 4 shows plots for the corresponding results. The variation of A^* as a function of U^* is consistent with previous experiments at low values of mass–damping (see, e.g., Khalak & Williamson 1996, 1997; Govardhan & Williamson 2000; Branković & Bearman 2006; Zhao *et al.* 2014*a*). Using the terminology in these previous works and the observed variation of the response amplitude, we have identified the initial, upper, lower, and desynchronization branches as listed in Table 1. Two more regions at the lower and upper ends of the reduced velocity range where response amplitudes are very low have also been included for completeness. In addition, a ‘bistable region’ that marks the transition between the upper and lower branches has also been included, as this will be discussed separately. The plot includes the envelope bracketing the top and bottom 5% levels of amplitudes recorded at each reduced velocity. The width of the envelope shows that amplitude modulations are pronounced in the middle of the initial branch ($3.7 < U^* < 4.2$) and in the second half of the upper branch ($5.7 < U^* < 6.8$) comparatively to the remaining regions.

As seen in the bottom plot in figure 4, f^* increases monotonically from 0.65 to 1.58 from the lowest to the highest U^* value. In the initial, upper, transition, and lower branches the frequency of the transverse force, $f_{C_y}^*$, is almost equal to f^* , except for the second half of the upper branch ($5.7 < U^* < 6.8$) where $f_y^* > f^*$. However, it should be noted

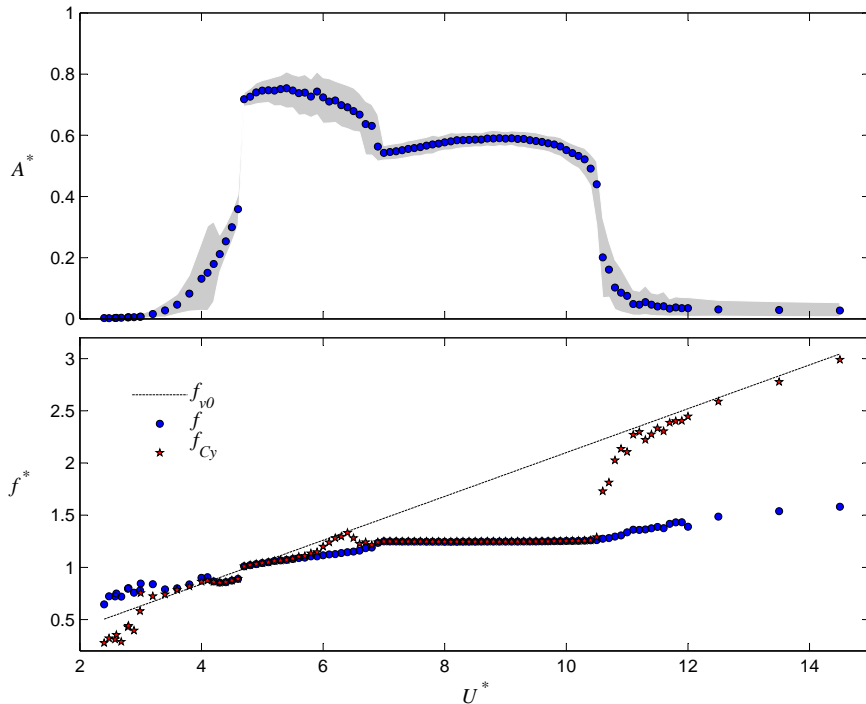


FIGURE 4. Variation of the normalized mean amplitude, A^* , and frequency, f^* , of cylinder response and frequency of the transverse force, f_{Cy}^* , with reduced velocity, U^* ; $m^* = 3.00$; $\zeta = 0.0035$. The dashed line indicates the frequency of vortex shedding from a stationary cylinder f_{v0} assuming a constant Strouhal number of 0.208. Amplitudes are normalized by the cylinder diameter and frequencies by the natural frequency in still water.

upfront that the instantaneous phase difference between force and displacement exhibits irregular behaviour in the latter range as will be explicitly shown further below. As a consequence, mean values of f_{Cy}^* , which are obtained by time averaging the instantaneous frequency, may be vague in the second half of the upper branch and should be interpreted with caution. In the lower branch, f^* remains constant at approximately 1.25, which is comparable to 1.275 predicted using the empirical formula (eq. 1.7) given by Govardhan & Williamson (2000). Overall, the variation of the response frequency with the reduced velocity is consistent with previous experiments at low values of mass-damping (Khalak & Williamson 1997; Govardhan & Williamson 2000; Zhao *et al.* 2014a).

In the following, we focus on the phase dynamics by presenting time series of the instantaneous phase difference between the transverse force and the displacement. At the lower and higher ends of the reduced velocity range, the instantaneous phase displays highly random fluctuations due to the absence of synchronization, which are not shown for economy of space. Figure 5 shows the normalized phase ϕ^* at five different reduced velocities within the synchronization range. At the start of the initial branch ($U^* = 3.2$), the phase displays some random fluctuations about the zero level whereas in the middle of the initial branch the fluctuations about the mean level become quasi-periodic ($U^* = 4.0$). This quasi-periodicity subsides towards the end of the initial branch where the phase stabilizes at $\phi^* \approx 0$. At the start of the upper branch ($U^* = 5.0$) the phase remains stable, i.e. the transition from the initial branch to the upper branch does not involve any marked change in the phase dynamics. In the middle of the upper branch ($U^* = 6.1$),

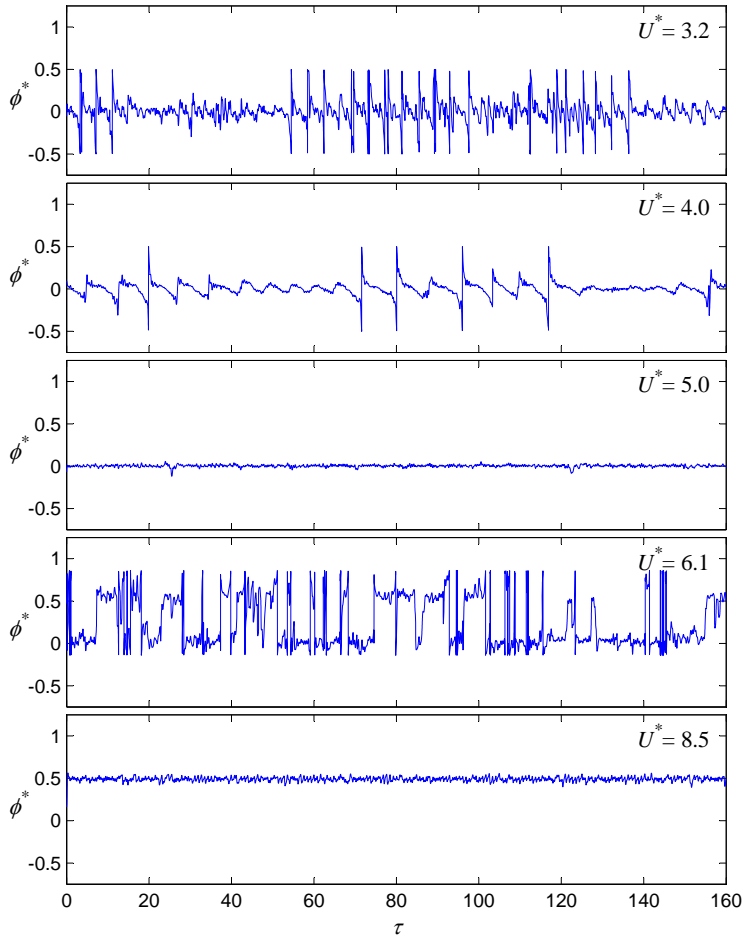


FIGURE 5. Time series of the instantaneous phase difference between transverse force and displacement at five reduced velocities; initial branch: $U^* = 3.2$ and 4.0 ; upper branch: $U^* = 5.0$ and 6.1 ; lower branch: $U^* = 8.5$. The normalized phase, ϕ^* , is wrapped in the interval $[-1, 1]$ except for $U^* = 6.1$ where the phase is wrapped in the interval $[-1/6, 5/6]$ for improved visualization.

ϕ^* intermittently switches between levels of approximately 0 and 0.5 at random instants. The random phase jumps persist in the second half of the upper branch ($5.7 < U^* < 6.8$). At $U^* = 8.5$, the phase difference remains remarkably stable around $\phi^* \approx 0.5$ ($\phi \approx 180^\circ$), which is typical throughout the lower branch.

Figure 6 shows time series of the phase difference exclusively in the upper branch. At the beginning of the upper branch ($U^* = 4.8$), the instantaneous phase remains stable at $\phi^* \approx 0$. With increasing the reduced velocity, sudden phase jumps to the $\phi^* \approx 0.5$ level become more and more frequent ($U^* = 5.3, 5.8, \text{ and } 6.3$). At the end of the upper branch ($U^* = 6.8$) the instantaneous phase stabilizes at $\phi^* \approx 0.5$ barring few occasional excursions to the zero level. The random phase dynamics observed near the middle of the upper branch may reflect the chaotic character of vortex-induced vibration discovered by Zhao *et al.* (2014b). However, a question that arises is whether sudden jumps in the phase difference are caused by some drastic changes in the flow dynamics, such as instantaneous swaps in the phasing of vortex shedding induced by sudden changes in the mode of vortex

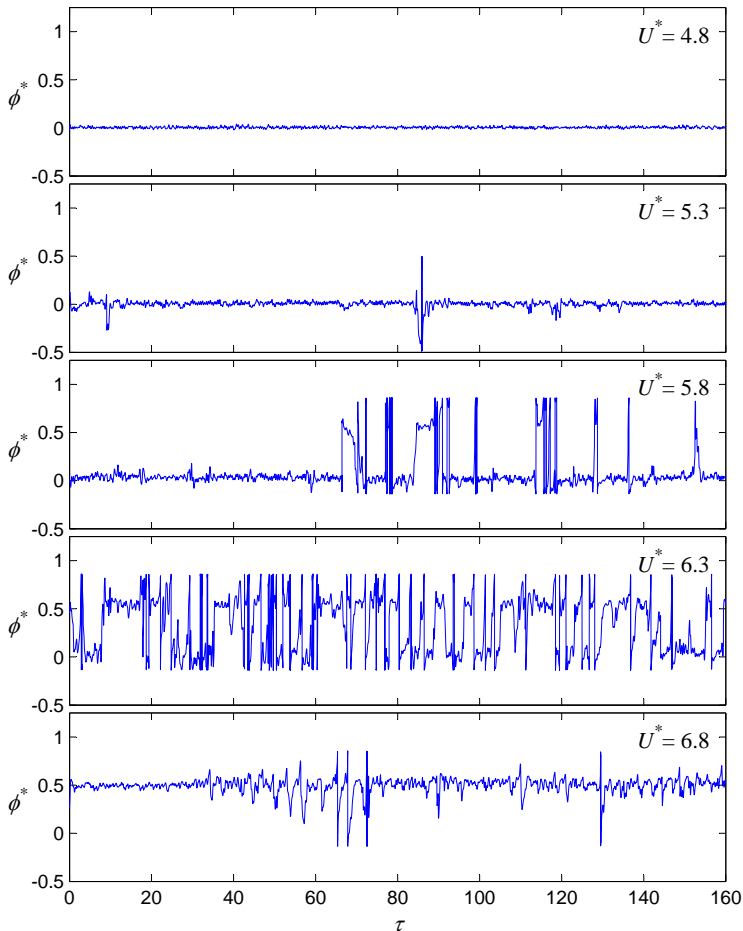


FIGURE 6. Time series of the instantaneous phase difference between transverse force and displacement at different reduced velocities in the upper branch: $U^* = 4.8, 5.3, 5.8, 6.3,$ and 6.8 . The normalized phase is wrapped in the interval $[-1, 1]$ except for $U^* = 5.8$ and 6.3 where the phase is wrapped in the interval $[-1/6, 5/6]$.

shedding. Most likely, such physical changes require finite time to take place, e.g. shed vortices cannot suddenly swap positions on different sides of the wake. Thus, it seems more likely that small variations in the phasing of vortex shedding are responsible for the sudden jumps in instantaneous ϕ . Leontini *et al.* (2006b) nicely illustrated how small changes in the pressure balance between the effective stagnation point and low pressure region due to vortices in the formation region can result in 180° changes in ϕ .

Figure 7 shows time series of the unwrapped phase for the same reduced velocities in the upper branch as in figure 6. Now, it can be clearly seen that, e.g. at $U^* = 5.8$, the unwrapped phase displays sudden jumps by $\Delta\phi^* = \pm n$, where n is a small integer number, typically 1 or 2. This corresponds to periods of almost constant phase $\phi^* \approx 0$ and phase slips in-between. This indicates intermittent phase dynamics, a feature which typically marks the transition in the border of synchronization (Pikovsky *et al.* 2001). We may argue that ϕ is effectively constant at $U^* = 5.8$. When U^* increases to 6.3 , ϕ^* drifts continuously resulting in an unbounded growth. The drifting behaviour prevails in the second half of the upper branch, i.e. over the range $6.0 < U^* < 6.8$. In the context

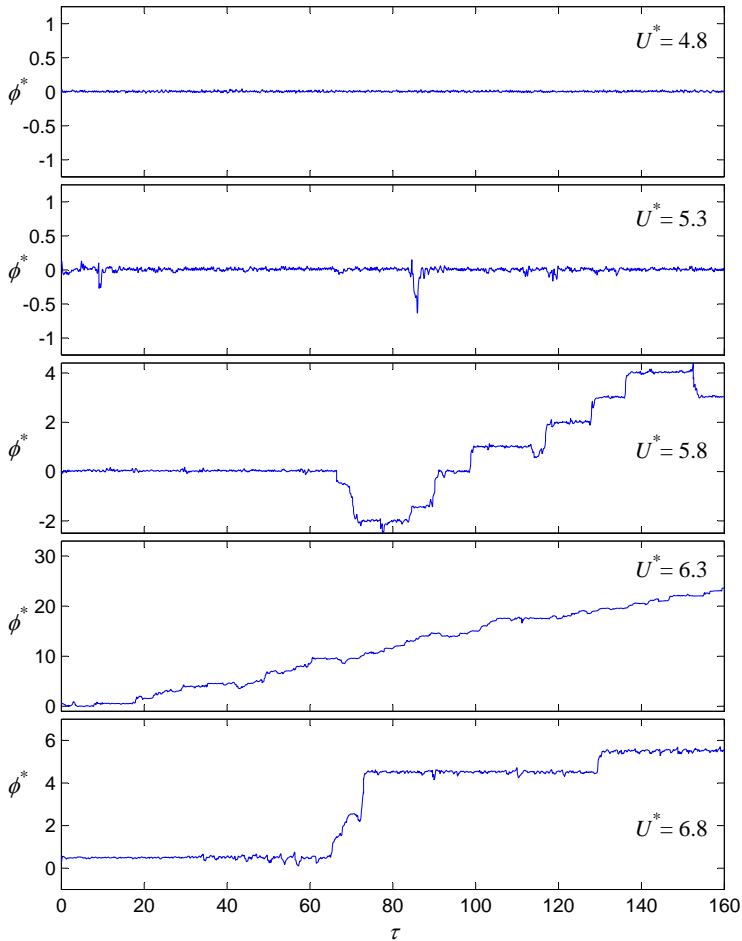


FIGURE 7. Time series of the unwrapped phase difference between transverse force and displacement at different reduced velocities in the upper branch: $U^* = 4.8, 5.3, 5.8, 6.3,$ and 6.8 .

of nonlinear dynamics, the continuous drift in phase corresponds to the loss of phase locking, i.e. loss of synchronization (Pikovsky *et al.* 2001). Once the bistable region is entered at $U^* = 6.8$, periods of effectively constant phase re-emerge with phase slips separating them. As shown earlier, after the upper \leftrightarrow lower transition is completed, the phase difference remains very stable at $\phi^* = 0.5$, i.e. synchronization is re-established in the lower branch. Although the time series of the unwrapped phase do provide some complimentary information, the phenomenological loss of phase locking in part of the upper branch cannot be accounted for.

Table 2 summarizes the main observations on the basis of the instantaneous phase difference between transverse force and displacement. It is interesting to note that the ranges of different phase dynamics do not correspond to the response branches identified from the variation of amplitude with reduced velocity shown in table 1.

On closing this section, the variation of the time-averaged phase difference between force and displacement as a function of the reduced velocity is presented in figure 8. The mean phase difference remains slightly above zero from the initial branch up to the middle of the upper branch where it rapidly changes by approximately 180° within the range

Range	Phase dynamics	Branch(es)
$3.2 \leq U^* < 3.8$	fairly stable with distinct jumps (phase slips)	initial
$3.8 \leq U^* < 4.3$	quasi-periodic	initial
$4.3 \leq U^* < 5.5$	stable	initial+upper
$5.5 \leq U^* < 6.1$	stable with distinct jumps (phase slips)	upper
$6.1 \leq U^* < 6.7$	drifting	upper
$6.7 \leq U^* < 7.0$	stable with distinct jumps (phase slips)	transition
$7.0 \leq U^* < 10.5$	very stable	lower
$10.5 \leq U^* < 11.1$	random	desynchronization

TABLE 2. Response characteristics based on the instantaneous phase difference between transverse force and displacement.

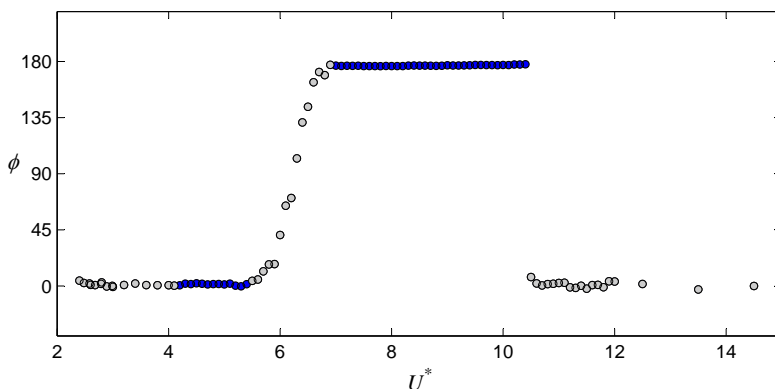


FIGURE 8. Variation of the time-averaged phase lag ϕ between transverse force and displacement as a function of U^* . Grey-filled symbols indicate cases for which the instantaneous phase exhibits intermittent jumps and/or continuous drifting and therefore it is not appropriate to characterize the phase dynamics solely by a single time-averaged value.

$5.5 < U^* < 6.7$. It then remains just below 180° throughout the lower branch. Grey-shaded symbols denote points where the time-averaged value of the phase difference cannot appropriately characterize the dynamics due to sudden jumps or continuous drifting of the instantaneous phase. This occurs in the lower and upper ends of the reduced velocity range and in the second half of the upper branch as has been discussed above.

4.2. Indirect measurements

In this section, we characterize the hydrodynamics of the freely oscillating cylinder in terms of the drag and lift components of the total force. Prior to the presentation of the phase dynamics, we present results for the magnitude and frequency of the lift and drag components. Figure 9 shows the variation of the lift magnitude C_L and frequency f_L^* with reduced velocity U^* . The lift magnitude increases steeply with U^* in the initial branch. At the end of the initial branch C_L jumps to a maximum value of 2.8 at the start of the upper branch. Subsequently, C_L decreases rather steeply over the entire upper branch. The transition from the upper to the lower branch is nearly continuous but is marked by an upward kink and a notable change in the rate of decrease of C_L with U^* . The end of the lower branch is clearly marked by a sudden drop in magnitude. The C_L plot includes the envelope of the 95% confidence band of magnitudes recorded at each reduced velocity.

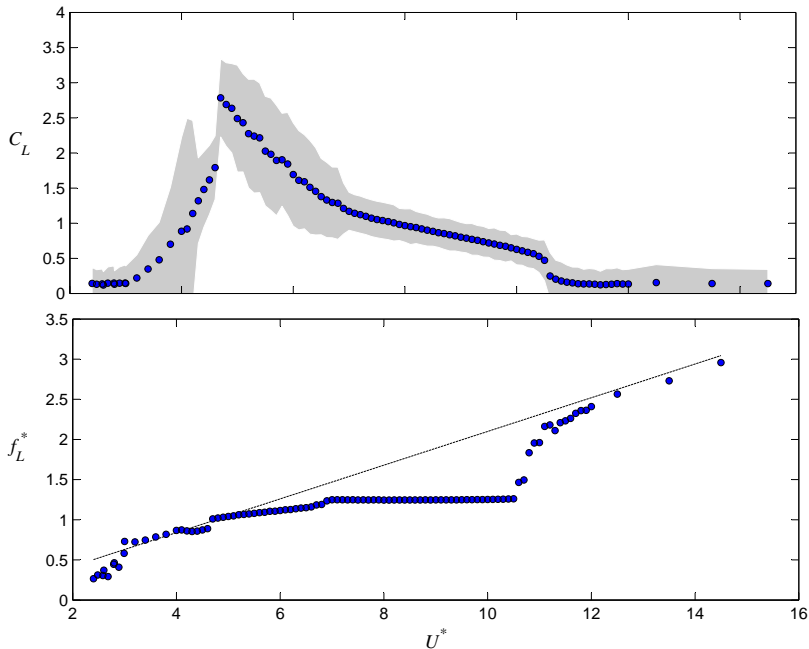


FIGURE 9. Variations of the mean lift magnitude C_L (top plot) and mean frequency f_L^* (bottom plot) with U^* . Data represent the time-averaged values of the corresponding time series. In the top plot, the shaded area indicates the 95% confidence band of magnitudes recorded at each U^* .

Clearly, the envelope indicates that modulations in C_L are pronounced in the region of quasi-periodic response in the initial branch. In contrast, the envelope is narrow at the end of the initial branch. The envelope becomes comparatively wide in the upper branch, which indicates the existence of considerable magnitude modulations. The bottom plot in figure 9 shows the variation of the lift frequency f_L^* . Contrary to the abnormal variation of the frequency of the transverse force in the second half of the upper branch (see figure 4), f_L^* is perfectly synchronized with the cylinder motion and continuously increases over the entire upper branch. In the lower branch, f_L^* remains constant at a level as if the frequency is limited by some factor. Outside the synchronization region, f_L^* tends to follow the line corresponding to a constant Strouhal number.

Figure 10 shows that the mean value of the drag component $C_{D_{\text{mean}}}$ attains a peak value of approximately 2.07 at $U^* = 5.3$, approximately where the peak response amplitude occurs. Generally, $C_{D_{\text{mean}}} \propto A^*$ in the upper branch. The mean drag coefficient is remarkably low before the initial branch. Transitions between initial \leftrightarrow upper and upper \leftrightarrow lower branches are marked by distinct jumps in $C_{D_{\text{mean}}}$, excluding data points in the bistable region where each stable state is characterized by distinct $C_{D_{\text{mean}}}$ values. In the lower branch $C_{D_{\text{mean}}}$ decreases gradually with U^* to a constant level that corresponds to approximately the conventional drag coefficient from a non-oscillating cylinder at corresponding Reynolds numbers. The magnitude of fluctuations of the unsteady drag component, C_D , attains a peak value of 0.40 at the start of the upper branch while its variation matches that of C_L as a function of U^* (cf. figure 9). This may account for the fact that fluctuations in both lift and drag originate from the unsteadiness of the flow due vortex shedding in the wake. Generally, the magnitude of the unsteady drag C_D is much lower than C_L and $C_{D_{\text{mean}}}$ values as might be expected from results for stationary cylinders.

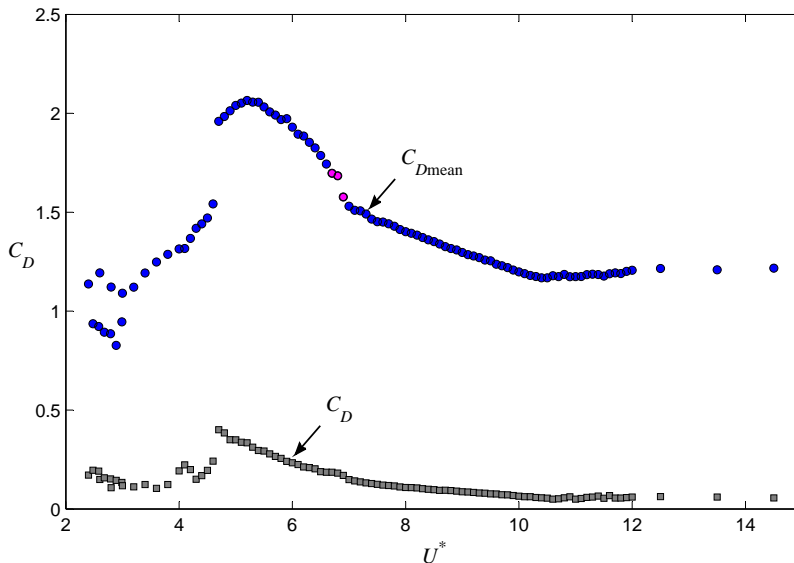


FIGURE 10. Variations of the mean drag $C_{D\text{mean}}$ and the magnitude of unsteady drag C_D with U^* . Data points marked by magenta colour correspond to the bistable region.

The time series of the indirectly-measured lift component were also processed using the Hilbert transform. Figure 11 shows the instantaneous phase difference of the lift with respect to the cylinder displacement, ϕ_L^* (normalized), at different reduced velocities. At $U^* = 3.2$ and 4, the dynamics is similar as that of the phase of the transverse force, ϕ^* (cf. figure 5). This is attributable to the fact that $F_L(t) \approx F_y(t)$ at very small effective angles of attack. At $U^* = 5$ and 6.1, ϕ_L^* remains stable in contrast to the time traces of ϕ^* which display random intermittent jumps at the same reduced velocity (cf. figure 6). In fact, ϕ_L^* remains very stable throughout the upper branch as shown in more detail in figure 12. This stands in sharp contrast to the existence of sudden jumps and/or continuous drifts of ϕ^* in the upper branch (cf. figure 7). It should be noted here that the time series of the unwrapped phase of the lift do not differ from the time series of the wrapped phase in the entire upper branch. Furthermore, ϕ_L^* also remains very stable across the entire lower branch as shown, for example, at $U^* = 8.5$ in figure 11. Therefore, we see that the phase difference between lift and displacement exhibits well-behaved dynamics throughout the synchronization range.

As discussed above, the instantaneous phase difference between lift and displacement remains bounded from the middle of the initial branch till the end of the lower branch ($4.2 \leq U^* \leq 10.5$). This phase locking can also be described in terms of frequency locking both of which are hallmarks of synchronization of an oscillator (elastically-mounted cylinder) to external forcing (lift) in the context of nonlinear dynamics (Pikovsky *et al.* 2001). The synchronization region can be clearly identified in the plot of $f^* - f_L^*$ versus f_L^* in figure 13. The external force entrains the frequency of the oscillator so that f^* becomes equal to f_L^* when the ‘detuning’ is sufficiently small; the detuning is generally defined as the absolute difference between the frequencies of the external force and of the natural frequency of the system, e.g. $|f_L^* - 1|$. Typically, the detuning is zero in the middle of the synchronization region for constant forcing amplitude. However, the forcing amplitude C_L is not constant here because the cylinder motion has a feedback effect on the external forcing. Thus, it becomes difficult to infer, from figure 13 alone, where the middle of the

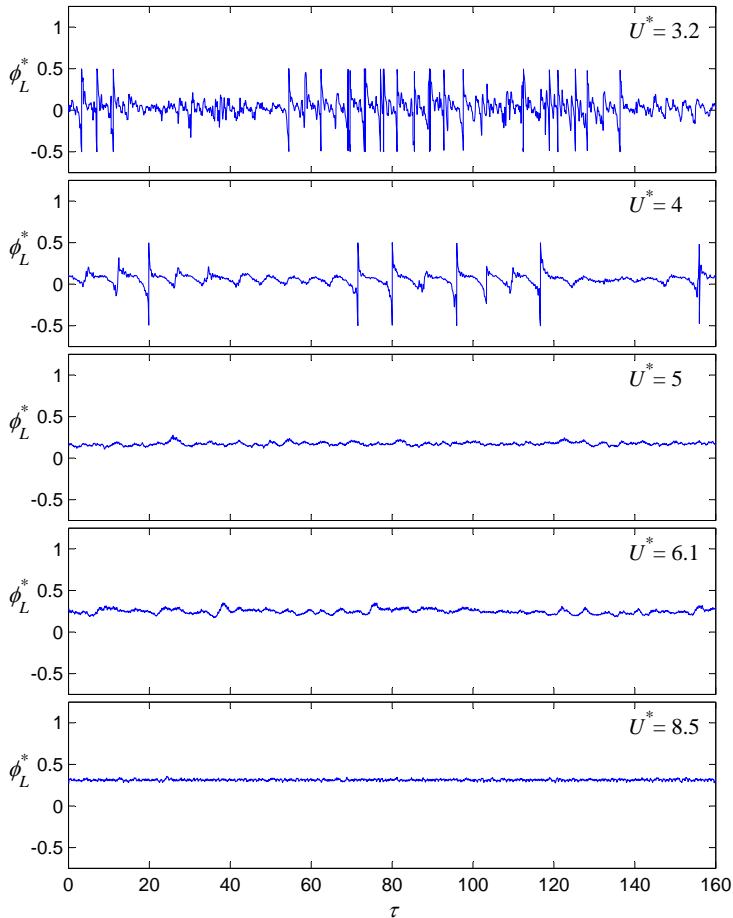


FIGURE 11. Time series of the instantaneous phase difference between the lift component and the displacement at different reduced velocities; initial branch: $U^* = 3.2$ and 4.0 ; upper branch: $U^* = 5.0$ and 6.1 ; lower branch: $U^* = 8.5$. The normalized phase is wrapped in the interval $[-0.5, 0.5]$. In these cases, the unwrapped phase is virtually the same except for $U^* = 3.2$ and 4 in which cases there exist some phase jumps.

synchronization region is and thereby what the true natural frequency of the oscillator is. For large detunings above a threshold, synchronization cannot be realized and the oscillator (cylinder) and the forcing (lift) have different frequencies.

Within the synchronization region, $F_D(t)$ fluctuations have a predominant frequency component at twice the frequency of the lift fluctuations. In addition, the relative velocity of the cylinder with respect to the free stream, $U(t)$, fluctuates at twice the frequency of cylinder oscillation. As a result of frequency locking, $F_D(t)$ and $U(t)$ fluctuate at the same frequency of $2f^*$. Thus, it is possible to compute the instantaneous difference of the phases of $F_D(t)$ and of $U(t)$, which is denoted as ϕ_D . At this point, it should be noted that the drag signal is affected more by electronic noise in the direct measurements of the forces because drag fluctuations generally have relatively small magnitude as shown earlier. In addition, the relative velocity is also prone to noise propagation due to the required differentiation, in time, of the displacement signal. Bearing in mind that the instantaneous phases of $F_D(t)$ and of $U(t)$ are affected by the above factors, figure 14 shows time series of their normalized phase difference, ϕ_D^* , at different U^* values in the

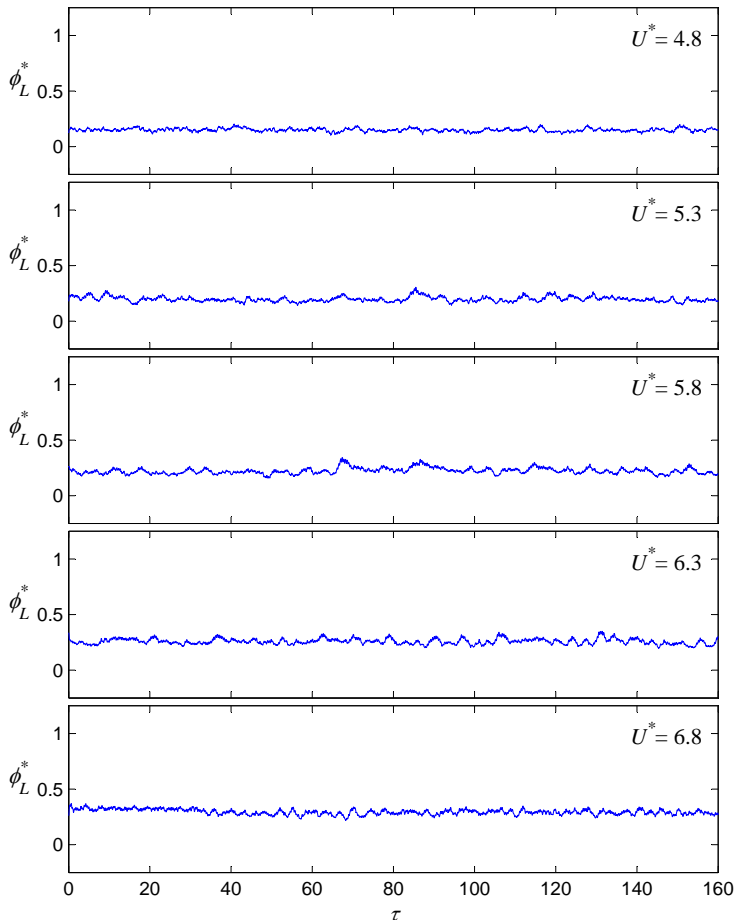


FIGURE 12. Time series of the instantaneous phase difference between the lift component and the displacement at different reduced velocities in the upper branch: $U^* = 4.8, 5.3, 5.8, 6.3,$ and 6.8 . The wrapped and unwrapped phases are virtually the same in all cases.

synchronization region. In the initial branch, ϕ_D^* changes continuously without apparent periods of synchronous phase. In the upper and lower branches, ϕ_D^* displays periods of synchronous phase separated by phase slips. At $U^* = 6.1$, the periods of synchronous phase alternate relatively quickly so that the ϕ_D^* displays a decreasing trend. In the lower branch, the periods of synchronous phase are re-established with phase slips separating them. Generally, ϕ_D is sufficiently stable within the synchronization region so that the mean phase difference can be estimated to an acceptable degree of uncertainty.

Figure 15 shows the mean values of ϕ_L and ϕ_D as functions of U^* . Although data points are included for the entire range of reduced velocities examined, it should be remembered that mean values of ϕ_L are accurate within the range $3.2 \leq U^* < 10.5$ whereas mean values of ϕ_D are fairly accurate within a narrower range $4.3 \leq U^* < 10.1$. The mean phase of the lift with respect to the displacement, ϕ_L , increases slowly in the initial branch from nearly zero. The transition from the end of initial branch to the start of the upper branch is marked by a distinct jump from $\phi_L = 23^\circ$ to 45° , which nearly corresponds to a doubling in the phase difference. In the upper branch and in the transition region, ϕ_L increases almost linearly with U^* . The transition from the end of

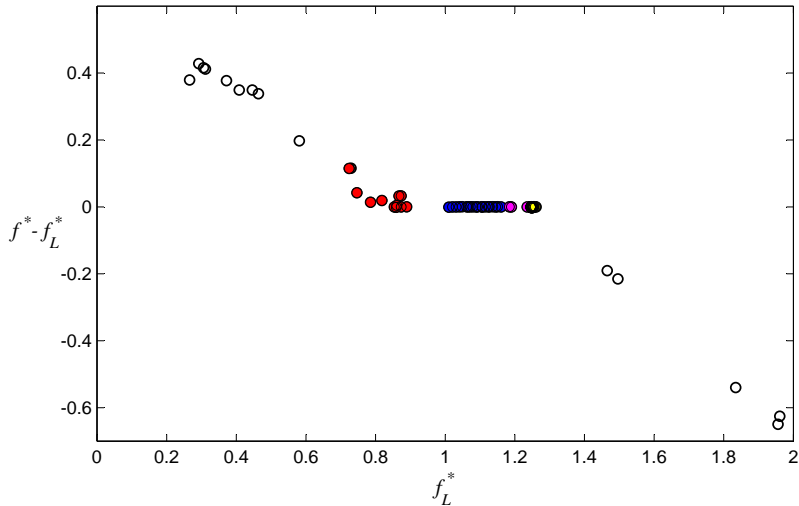


FIGURE 13. (Colour online) Difference of the frequencies of the cylinder oscillation, f^* , and the lift forcing, f_L^* , as a function of f_L^* illustrating the synchronization region. Filled colours denote different response branches: initial (red), upper (blue), transition (magenta), lower (yellow). Note that data points in the lower branch fall on top of each other.

the upper branch to the start of the lower branch, excluding three data points in the transition region, involves a second distinct jump from $\phi_L = 103^\circ$ to 122° . In the lower branch, ϕ_L remains remarkably constant. The mean phase of the drag component with respect to the relative velocity ϕ_D increases slowly in the first half of the initial branch followed by a steep increase in the second half of the initial branch at the end of which it attains a maximum value of 107° . Subsequently, ϕ_D decreases smoothly in the first half of the upper branch whereas in the second half ϕ_D appears to remain relatively constant at around $\phi_D \approx 50^\circ$. In the latter range, ϕ_D values have relatively larger uncertainty due to the existence of repeated phase slips. Nevertheless, the variation of ϕ_D illustrates the ‘irregular’ phase dynamics in the second half of the upper branch. Finally, from the start of the upper branch till the end of the lower branch, ϕ_D decreases rather smoothly with the reduced velocity from approximately 90° to 0° .

From nonlinear dynamical systems it is known that frequency and phase of an oscillator are closely related since the phase typically changes by 180° as the forcing frequency varies across the synchronization range (Pikovsky *et al.* 2001). Indeed, we have actually seen this in figure 8. However, this change takes place over a range of reduced velocities where the instantaneous phase difference between $F_y(t)$ and $y(t)$ becomes unbounded due to continuous drifting. Therefore, the mean phase ϕ takes intermediate values between 0° to 180° , which are vague; the dynamics become irregular and the phase of the transverse force with respect to the cylinder oscillation cannot be unambiguously correlated with the synchronization frequency within the former range. In contrast, the phase difference between lift and displacement ϕ_L varies in an orderly fashion with the lift frequency as shown in figure 16. Prior to the onset of synchronization at low f_L^* values ϕ_L remains at a low level close to zero. For f_L^* values above the synchronization region, ϕ_L decreases smoothly towards the zero level. Data points in the synchronization range, whose borders have been marked by vertical lines on the plot, have a linear correlation coefficient of 0.9889, which indicates a strong linear relationship between f_L and ϕ_L . In the lower branch where f_L^* remains almost constant, ϕ_L also remains almost constant so that data

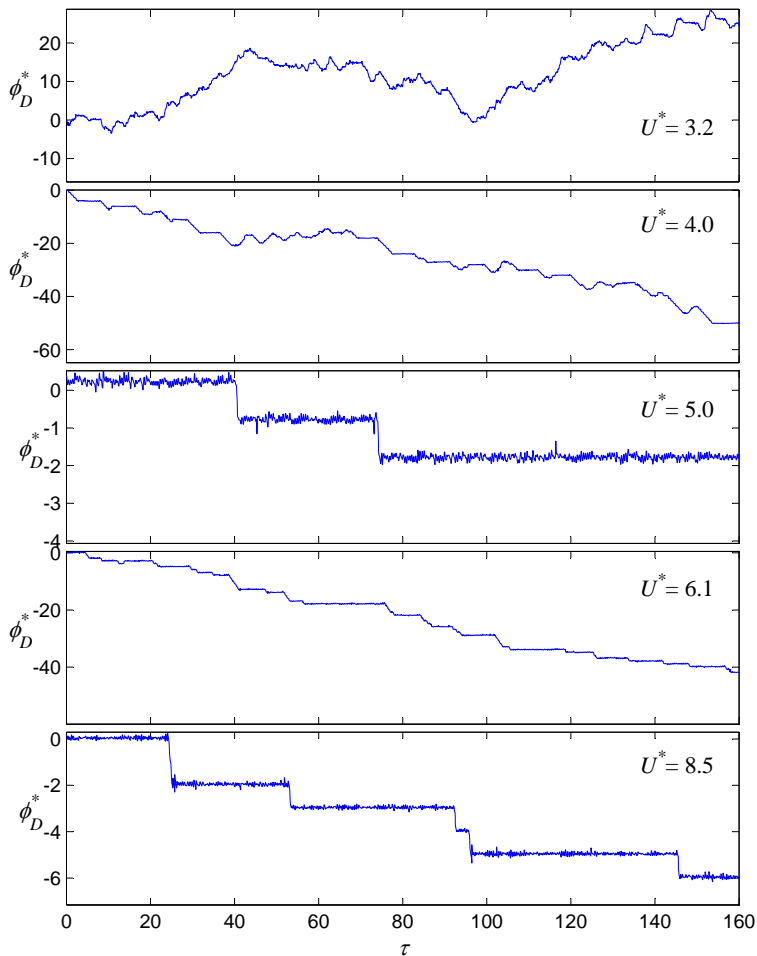


FIGURE 14. Time series of the instantaneous phase difference (unwrapped) between the drag component and the relative velocity at different reduced velocities in the synchronization region; initial branch: $U^* = 3.2$ and 4.0 ; upper branch: $U^* = 5.0$ and 6.1 ; lower branch: $U^* = 8.5$.

points fall on top of each other (agglomerated data points at maximum ϕ_L values). Another point to note is that transitions from the initial to the upper branch as well as from the upper to the lower branch are clearly marked by simultaneous jumps in both frequency and phase of the lift (excluding points in the bistable region).

The variation of ϕ_L as a function of f_L^* shown in figure 16 suggests that the lift phase unequivocally depends on the lift frequency which is the same as the frequency of vortex shedding in the wake during synchronization. This relationship between the lift phase and the frequency of vortex shedding has been previously examined in detail by Konstantinidis & Liang (2011). They showed that a direct relationship exists between the phase of the lift and the timing of vortex shedding for the case of synchronization of the cylinder wake to external forcing by means of periodic perturbations in the velocity of the free stream. Furthermore, Konstantinidis & Bouris (2016) showed how the kinematics of a cylinder oscillating transversely to a free stream can be analysed in terms of the relative velocity of the cylinder and the free stream. Therefore, it is reasonable to assume that the phase of the lift component on a cylinder oscillating transversely to a free stream directly

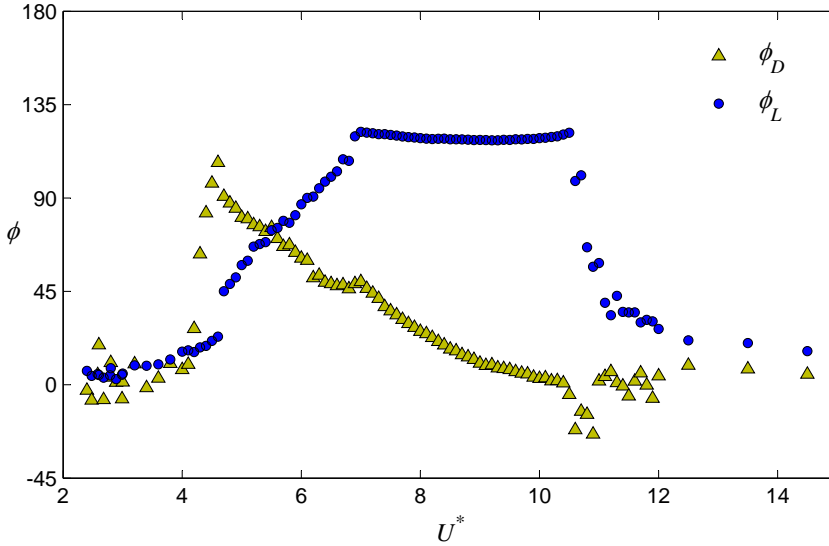


FIGURE 15. Variations of mean phase differences between drag and relative velocity, ϕ_D , and between lift and displacement, ϕ_L , with reduced velocity, U^* . Mean values are given in degrees.

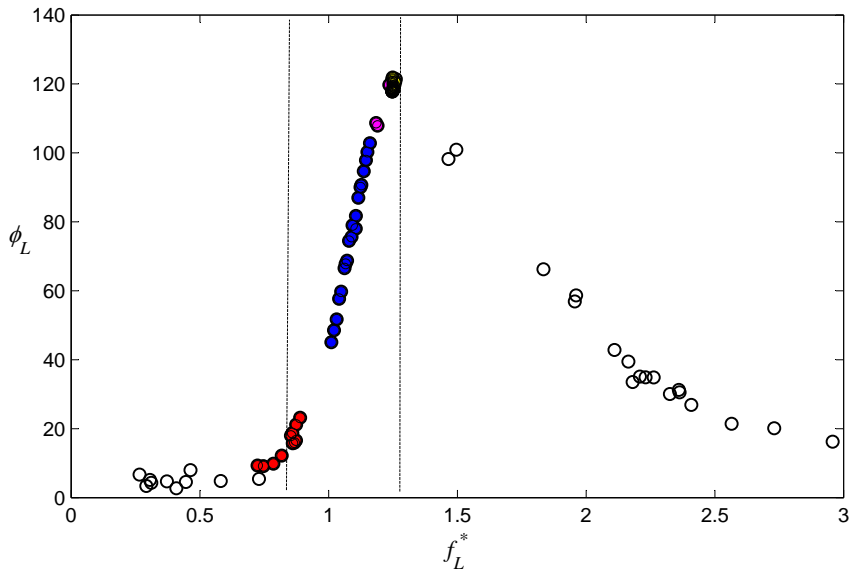


FIGURE 16. (Colour online) Variation of the lift phase, ϕ_L , with the lift frequency, f_L^* . Filled colours denote different response branches: initial (red), upper (blue), transition (magenta), lower (yellow). Note that data points in the lower branch cannot be discerned as they fall on top of each other. Vertical dashed lines mark the borders of the synchronization region.

reflects the vortex dynamics in the wake, which has been the founding hypothesis for the present study.

As discussed earlier, the phase dynamics of lift exhibits a notable change in the second half of the upper branch compared to the first half. This change can also be illustrated by another metric: the variation of the standard deviation of the instantaneous ϕ_L , denoted

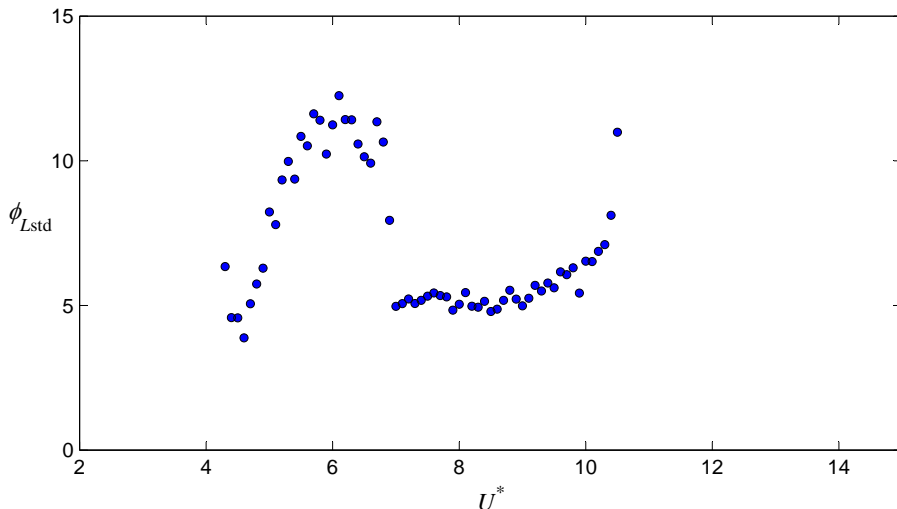


FIGURE 17. The variation of the standard deviation of the lift phase, ϕ_{Lstd} , with reduced velocity, U^* .

as ϕ_{Lstd} . The variation of ϕ_{Lstd} as a function of U^* is shown in figure 17. Data points cover the last part of the initial branch and the entirety of the upper and lower branches where strong phase-locking occurs. For U^* values in the first half of the initial branch, ϕ_{Lstd} is very large (exceeds the scale of the plot) but then drops and attains a minimum value at the end of the initial branch as seen in the plot. Subsequently, ϕ_{Lstd} increases rapidly in the first half of the upper branch whereas ϕ_{Lstd} stays at a high level above 10° in the second half of the upper branch. In the lower branch, ϕ_{Lstd} drops to a low constant level of approximately 5° . Towards the end of the lower branch ϕ_{Lstd} increases rapidly with U^* and ϕ_{Lstd} exceeds the scale of the plot outside the synchronization region. Therefore, the ϕ_{Lstd} results show that the phase difference between lift and displacement displays relatively pronounced modulations in the second half of the upper branch. Overall, the standard deviation of ϕ_L is small in the synchronization region, which reflects the absence of jumps and/or drifts in ϕ_L , i.e. the phase difference of the lift component with respect to the cylinder oscillation provides a robust indicator of the dynamics.

4.3. Physical function of drag and lift components

To understand the physical function of the drag and lift components in VIV, we can take their instantaneous projections on the direction of cylinder motion (y axis) using the following relationships,

$$F_{Dy} = -F_D \sin a_{\text{eff}} \quad \text{and} \quad F_{Ly} = F_L \cos a_{\text{eff}}. \quad (4.1a, b)$$

Next, we process the time series of $F_{Dy}(t)$ and $F_{Ly}(t)$ using the Hilbert transform as we did earlier with the time series of $F_D(t)$ and $F_L(t)$. However, both $F_{Dy}(t)$ and $F_{Ly}(t)$ are now synchronized with the cylinder motion due to their explicit dependency on a_{eff} . As a consequence, the differences of the instantaneous phases of $F_{Dy}(t)$ or $F_{Ly}(t)$ and of $y(t)$ are very stable in the initial, upper and lower branches, including the bistable region. Therefore, mean values of the instantaneous phase differences can be employed with confidence in order to reveal the functions of the drag and lift components. The corresponding phase differences are denoted ϕ_{Dy} and ϕ_{Ly} , respectively, and their variations with U^* are shown in figure 18. Two observations can be made immediately.

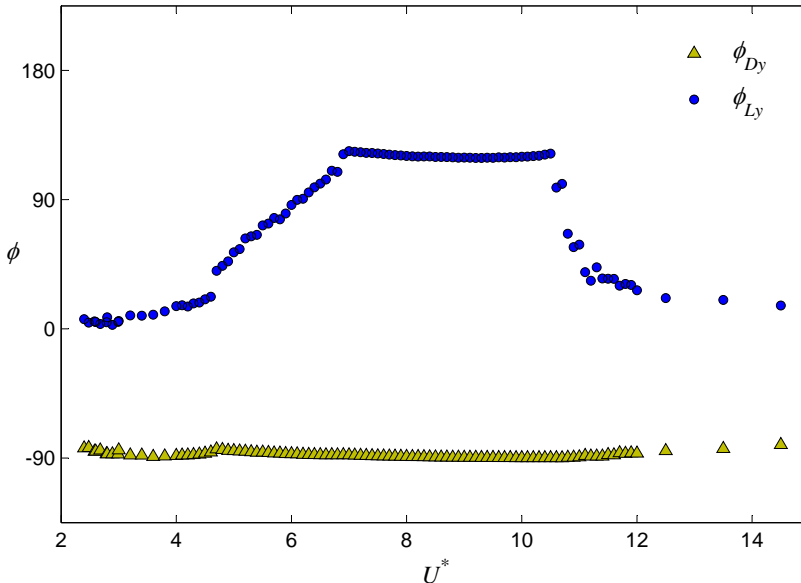


FIGURE 18. Variations of the phase differences ϕ_{Dy} and ϕ_{Ly} between $F_{Dy}(t)$ and $y(t)$ and between $F_{Ly}(t)$ and $y(t)$, respectively, with reduced velocity, U^* . Data show time-averaged mean values of the instantaneous phase differences obtained using the Hilbert transform of the corresponding signals.

First, ϕ_{Dy} remains very close to -90° over the entire U^* range. These results show that $F_D(t)$ makes a contribution that always opposes the velocity of the cylinder, predominantly due to the mean drag, i.e. the drag always makes a contribution to positive damping of the cylinder vibration as expected from purely theoretical considerations laid out in the Introduction. Second, at each reduced velocity $\phi_{Ly} \approx \phi_L$ (cf. figure 15). Thus, $F_L(t)$ induces a component along the direction of oscillation $F_{Ly}(t)$ that has the proper phasing in order to excite vortex-induced vibration.

Typically, the component of the force in-phase with the cylinder velocity $C_y \sin \phi$ is considered to be the excitation force coefficient in VIV. According to the equation of motion, $C_y \sin \phi \propto f^* A^* / U^{*2}$, where the proportionality factor is proportional to the damping ratio. For very low values of the damping ratio ζ , the proportionality factor is itself very low. This considerably limits the permissible range of values of the phase angle, i.e. ϕ has to be just above 0° or just below 180° . A very important finding from the present study, as illustrated in figure 19, is that the lift coefficient varies linearly with the same scaling factor as does the typical excitation coefficient. A best-linear fit to the data,

$$C_L = C_{L0} + \kappa \frac{f^* A^*}{U^{*2}}. \quad (4.2)$$

yields $C_{L0} = 0.1$ and $\kappa = 75.8$ with a R-square value of 0.9998, which reveals a highly linear relationship. This is a remarkable result since now there is no dependency on the phasing of the lift force. The constant factor, C_{L0} , corresponds to approximately the lift coefficient of a non-vibrating cylinder at similar Reynolds numbers. Generally, the value of C_{L0} is quite low compared to the values of the lift coefficient for oscillating cylinders and the first term in (4.2) can be neglected.

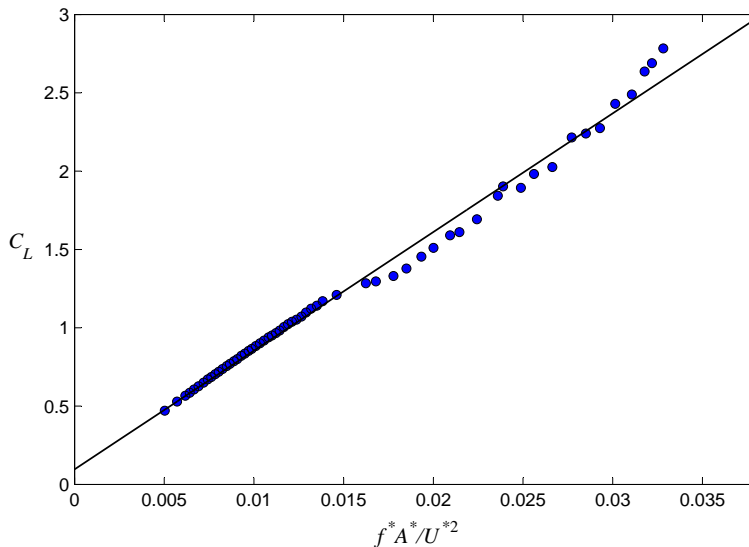


FIGURE 19. Variation of the lift coefficient C_L as a function of the parameter $f^* A^* / U^{*2}$ within the lower and upper branches. The straight line is a least-squares fit to the data, which has an R-square value of 0.9998 showing that the relationship is linear.

5. Modelling and further analysis

5.1. Modelling of hydrodynamics

The following expressions are introduced for modelling the lift and drag components of the total hydrodynamic force acting on a cylinder undergoing synchronized VIV

$$F_L(t) = \frac{1}{2} \rho U_\infty^2 DL C_L \sin(\omega t + \phi_L), \quad (5.1)$$

and

$$F_D(t) = \frac{1}{2} \rho U_\infty^2 DL [C_{D\text{mean}} + C_D \sin(2\omega t + \phi_D)], \quad (5.2)$$

respectively, where $\omega = 2\pi f$ is the angular frequency of cylinder oscillation in radians/s. Note that the lift fluctuates at the cylinder oscillation frequency whereas the drag fluctuates at twice the frequency of cylinder oscillation. The above expressions for the drag and lift arise naturally and also fully conform with the indirect measurements presented earlier. The hydrodynamic coefficients $C_{D\text{mean}}$, C_D , and C_L are assumed to depend primarily on the kinematical parameters of the cylinder motion, e.g. on the normalized amplitude, A^* , and the normalized frequency, f^*/U^* . The Reynolds number is also an influencing parameter whose effect will not be considered here since the VIV response seems to be relatively insensitive to this effect in the present study, i.e. transition to turbulence occurs in the shear layers separating from the cylinder.

The analysis of the hydrodynamics can be simplified using the approximations $\sin \alpha_{\text{eff}} \approx \dot{y}/U_\infty$ and $\cos \alpha_{\text{eff}} \approx 1$ valid for small effective angles of attack. This can be justified since the maximum α_{eff} value, which occurs at the start of the upper branch, is approximately 11° . Using the above approximations and assuming that the displacement is nearly sinusoidal, $y(t) \approx A \sin(\omega t)$, it can be readily shown that

$$\frac{F_{Ly}(t)}{\frac{1}{2} \rho U_\infty^2 DL} \approx C_L \sin(\omega t + \phi_L) + \dots, \quad (5.3)$$

and

$$\frac{F_{Dy}(t)}{\frac{1}{2}\rho U_\infty^2 DL} \approx - \left(\frac{\omega A}{U_\infty} \right) \left[C_{D\text{mean}} \cos(\omega t) + \frac{1}{2} C_D \sin(\omega t + \phi_D) + \dots \right], \quad (5.4)$$

where higher order harmonics of the primary frequency of cylinder oscillation have been neglected. From equation (5.3), it can be verified that $\phi_{Ly} \approx \phi_L$ in excellent agreement with the results in figures 15 and 18. That is, $F_{Ly}(t)$ has approximately the same phasing as $F_L(t)$ with respect to displacement, $y(t)$. Moreover, equation (5.4) shows that $F_{Dy}(t)$ comprises two separate contributions from the mean and the fluctuating drag. As seen in figure 10, C_D values are considerably less than $C_{D\text{mean}}$ values. Therefore, the sum in the square brackets of equation (5.4) is dominated by the first term related to the mean drag so that we can neglect, temporarily, the contribution of the fluctuating drag. This leads to

$$\frac{F_{Dy}(t)}{\frac{1}{2}\rho U_\infty^2 DL} \approx \left(\frac{\omega A}{U_\infty} \right) C_{D\text{mean}} \sin\left(\omega t - \frac{\pi}{2}\right), \quad (5.5)$$

where we have expressed the cosine function in terms of a sine function. A phase lag of $\phi_{Dy} \approx -\frac{\pi}{2}$ radians can be inferred from the above expression. So, in effect ϕ_{Dy} takes values close to -90° in excellent agreement with the results shown in figure 18. Thus, the above hydrodynamical model is consistent with measurements of the mean phases of lift and drag components and is employed in the following subsections to exemplify several aspects of VIV.

5.2. Chaotic oscillations in the upper branch

5.2.1. Phenomenology

The phenomenology of chaotic dynamics observed in the second half of the upper branch can be understood with the aid of phase diagrams of the F_{Ly} and F_{Dy} components of the hydrodynamic force shown in figure 20, where phasors (vectors) represent the magnitude and phase of each component with respect to the cylinder displacement (y axis) and velocity (\dot{y} axis). It is now important to take into account the influence of the fluctuating drag on the phase of F_{Dy} , whose value, according to the model equation (5.2), is given by

$$\phi_{Dy} = \arctan\left(1 + \frac{2C_{D\text{mean}}}{C_D \sin \phi_D}\right) \quad (5.6)$$

Since $\phi_{Dy} \approx -\pi/2$, we can use Taylor series expansion around this point to get

$$\phi_{Dy} = -\frac{\pi}{2} + \frac{1}{2} \frac{C_D}{C_{D\text{mean}}} \sin \phi_D + \dots, \quad (5.7)$$

where the series is truncated to the first order term. The second term on the right hand side is positive since $\phi_D \in [0^\circ, 90^\circ]$ in the upper and lower branches (see figure 15). Hence, we can see from equation (5.7) that the fluctuating drag results in a slight increase of ϕ_{Dy} above -90° . Indeed, measurements in figure 18 show that ϕ_{Dy} is few degrees above -90° in excellent agreement with the drag model. As a result, the angle of the phasor representing F_{Dy} remains approximately constant in the three different regions depicted in figure 20. In addition, ϕ_{Ly} is approximately equal to ϕ_L , which, as shown earlier, increases almost linearly with the reduced velocity in the upper branch. Thereby results the variation in the angle of the phasor representing F_{Ly} shown in figure 20. It should be noted that the magnitude of the phasors is not to scale for more lucid representation. The phasor of the resulting transverse force, which is the vectorial sum of the components of drag and lift in the direction of motion, is depicted in blue colour in figure 20.

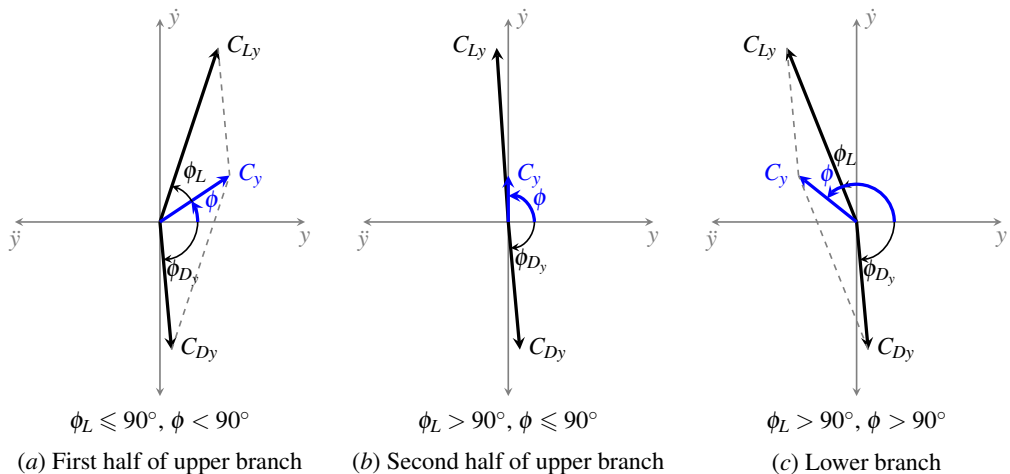


FIGURE 20. (Colour online) Phase diagrams of the drag and lift components of the transverse fluid force in three regions with different dynamics. The magnitude and angle of the phasors are not to scale for better visualization.

For reduced velocities in the first half of the upper branch, $\phi_L \leq 90^\circ$ and the resulting transverse force has a significant component in-phase with the cylinder velocity (figure 20a). As the reduced velocity is increased, ϕ_L quickly approaches to 90° in the middle of the upper branch. For reduced velocities in the second half of the upper branch, $90^\circ < \phi_L < 103^\circ$ and the phasors of F_{Ly} and F_{Dy} are pointing to approximately opposite directions in the phase diagram (figure 20b). As a result, they cancel each other out leaving a very small component of the transverse force almost in-phase with velocity. As the reduced velocity is increased further, ϕ_L jumps to 122° in the lower branch and the resulting transverse force now has a significant component in-phase with the acceleration of the cylinder.

When the phase difference between the forcing (i.e. the hydrodynamic lift) and the response (i.e. the cylinder motion) passes through the point where $\phi_L \approx 90^\circ$, the hydro-elastic system may be considered to be in a state of ‘unstable equilibrium’; although the phase difference between forcing and response ϕ_L remains bounded, small perturbations can cause amplitude modulations, i.e. perturbations have the largest impact in the system’s response (Pikovsky *et al.* 2001). Modulations in the amplitude of cylinder oscillation have a feedback effect on the fluid forcing causing the system to behave chaotically. This occurs at around $U^* \approx 6.1$, where $\phi_L = 90.05^\circ$ and $\phi_{L\text{std}}$ peaks (see figures 15 and 17), which supports our hypothesis. Furthermore, at approximately the same reduced velocity Zhao *et al.* (2014a) observed the chaotic nature of VIV for a similar hydro-elastic cylinder with a mass ratio of $m^* = 2.66$ (i.e. slightly lower than in the present study). When one looks at the instantaneous phase difference between transverse force and displacement, ϕ becomes unbounded because the forcing, i.e. C_y , is too weak; in this case, the system approaches a state of ‘neutral equilibrium’ for which the phase is ‘indifferent’ (Pikovsky *et al.* 2001). Not surprisingly, the continuous drifting of ϕ coincides with the region of a local minimum in C_y at around $U^* \approx 6.4$. Note that from the point of view of nonlinear dynamics, the relationship between $F_y(t)$ and $y(t)$ is governed by a different set of nonlinear equations than the relationship between $F_L(t)$ and $y(t)$; although the system’s response is common, the dynamics of each sub-system is different.

5.2.2. Revealing competing factors through formulae

The dynamics of VIV can be further illustrated through analytical formulae governing the hydrodynamics and the cylinder motion. From equations (5.3) and (5.4), we can express the component of the transverse force in phase with the velocity of the cylinder as

$$C_y \sin \phi = C_L \sin \phi_L - \frac{2\pi f^* A^*}{U^*} \left(C_{D\text{mean}} + \frac{1}{2} C_D \sin \phi_D \right). \quad (5.8)$$

Assuming that the cylinder displacement can be approximated, on the average, as sinusoidal $y(t) \approx A \sin(\omega t)$, the condition $C_y \sin \phi > 0$, which is required for positive excitation in free vibration (see Introduction), can be reformulated as

$$C_L \sin \phi_L > \frac{2\pi f^* A^*}{U^*} \left(C_{D\text{mean}} + \frac{1}{2} C_D \sin \phi_D \right). \quad (5.9)$$

The inequalities in (5.9) restrict the phase difference between lift and displacement in the range

$$\sin^{-1} \{W(A^*, f^*/U^*)\} < \phi_L < \frac{\pi}{2} - \sin^{-1} \{W(A^*, f^*/U^*)\}, \quad (5.10)$$

where

$$W(A^*, f^*/U^*) = \frac{2\pi f^* A^*}{U^*} \left(\frac{C_{D\text{mean}}}{C_L} + \frac{1}{2} \frac{C_D \sin \phi_D}{C_L} \right). \quad (5.11)$$

The term $W(A^*, f^*/U^*)$ represents a function of the normalized amplitude and frequency, which generally varies with the reduced velocity. The permissible range of ϕ_L values given by (5.10) is plotted along with ϕ_L measurements in figure 21. The permissible range of ϕ_L values becomes narrower as the reduced velocity is increased in the initial and in the first half of the upper branch ($4.7 \leq U^* < 6.1$). At the middle of the upper branch, $U^* \approx 6.1$, ϕ_L is restricted to be exactly 90° in agreement with indirect measurements. As discussed earlier, this point corresponds to the state of unstable equilibrium. In the second half of the upper branch, $W(A^*, f^*/U^*) \approx 1$ so that ϕ_L values should remain restricted to around 90° according to the restriction (5.10) posed by the equation of cylinder free motion. However, measurements show that ϕ_L continues to increase. In the lower branch, $7 \leq U^* < 10.5$, ϕ_L remains fairly constant and close to the upper limit of the permissible range.

In the upper branch, the frequency of oscillation increases while the relationship between ϕ_L and f^* is almost linear as discussed earlier with regard to figure 16. However, this variation of ϕ_L does not fully conform with the restriction posed by the equation of cylinder free motion as per (5.10), which restricts ϕ_L to values around 90° in the second half of the upper branch. This discrepancy may be explained by noting that the above restriction is based on the approximation of pure harmonic motion, which may not hold in the second half of the upper branch; as already pointed out, the latter range is characterized by considerable modulations in both the displacement and the fluid forcing. We interpret this as the result of competing factors posed by the hydrodynamics and the equation of cylinder free motion, which leads to deviations from the ideal harmonic motion. Moreover, the variation of the mean drag phase with reduced velocity in figure 15 shows that the ϕ_D remains approximately constant at a value of approximately 50° , which corresponds to the ϕ_D value at $U^* = 6.2$ where ϕ_L has a value equal to approximately 90° . This is consistent with the scenario of ‘irregular’ phase dynamics in the second half of the upper branch discussed above. Therefore, although the inequality in (5.10) is not strictly satisfied in the second half of the upper branch, the hydrodynamical model

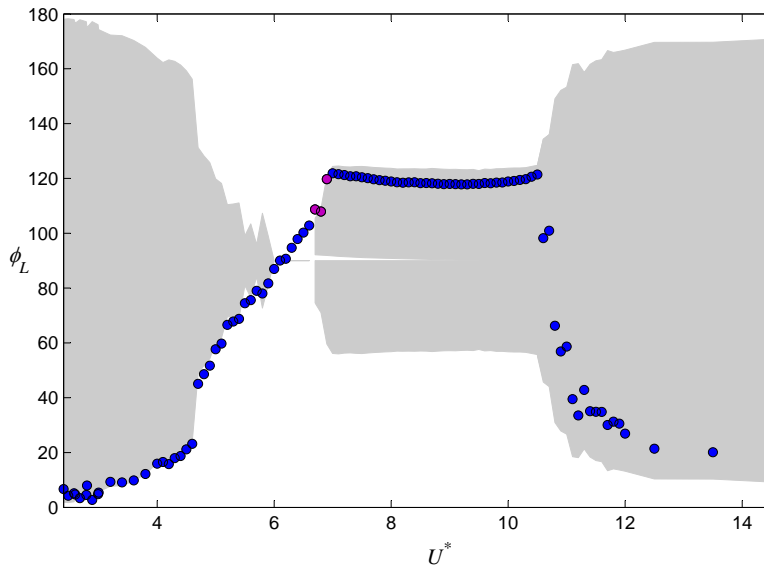


FIGURE 21. (Colour online) Permissible range of the phase difference ϕ_L as a function of the reduced velocity U^* computed from the inequalities in (5.10). Values of ϕ_L are in degrees. Magenta filling indicates points in the bistable range.

explains satisfactorily the experimental observations if probable deviations from the ideal harmonic oscillation are considered.

5.3. Response frequency in the lower branch – the lock-in region

The frequency of cylinder response remains approximately constant in the lower branch at a value close to the natural frequency of the hydro-elastic cylinder in still air, a phenomenon that is often referred to as ‘lock-in’ (Feng 1968) implying that the cylinder motion has taken over control of the vortex shedding. Nevertheless, previous studies as well as the present one at low values of mass and damping have clearly shown that the response frequency does not have to remain constant for strong two-way coupling between the cylinder motion and the vortex shedding, e.g. the response frequency increases in the upper branch. Thus, the constancy of the response frequency is a unique characteristic observed only in the lower branch. Since the phase difference and the common frequency of cylinder motion and fluid forcing must by default be related during synchronization, it follows that the phase difference must also remain constant in the lower branch if the response frequency remains constant. In this section, we clarify the reason why the phase difference between lift and displacement, and thereby the response frequency, both remain constant in the lower branch, or in other words, why a lock-in region exists.

The starting point is the requirement for positive excitation in free motion given by equation (5.9) and the fact that the lift coefficient is proportional to the combined parameter f^*A^*/U^{*2} as depicted by equation (4.2). Combining these two equations, we can arrive at

$$\left(C_{L0} + \kappa \frac{A^* f^*}{U^{*2}} \right) \sin \phi_L > \frac{2\pi f^* A^*}{U^*} (C_{D\text{mean}} + C_D \sin \phi_D). \quad (5.12)$$

The first term inside the parenthesis on the left-hand side and the second term inside the parenthesis on the right-hand side of (5.12) are small in comparison to the other terms inside the parentheses and can be neglected for simplicity without altering the essence

of the outcome. In the lock-in region (lower branch), ϕ_L is close to $\frac{\pi}{2}$ and using Taylor series expansion around this point yields $\sin \phi_L \approx 1 - \frac{1}{2}(\phi_L - \frac{\pi}{2})^2$. Substituting this into (5.12) and solving for ϕ_L after some rearrangements yields

$$\phi_L < \frac{\pi}{2} + \sqrt{2 \left(1 - \frac{2\pi}{\kappa} U^* C_{D_{\text{mean}}} \right)}, \quad (5.13)$$

where it has been assumed that ϕ_L is higher than $\frac{\pi}{2}$, which holds true in the lower branch. The outcome shows that ϕ_L becomes limited on the upper side. As U^* increases in the lower branch, the second term inside the parenthesis in the square root tends to become more negative and the value of the square root tends to decrease. However, the effect of increasing U^* is counterbalanced by an attendant decrease in $C_{D_{\text{mean}}}$ (see figure 10) so that the upper limit of ϕ_L stays at an almost fixed level, i.e. ϕ_L reaches a saturation level in the lower branch. This is tantamount to what has already been shown in §5.2.2 that the phase difference between lift and displacement is restricted by the equation of cylinder free motion and takes values close to the upper limit of the permissible range (see equation (5.10) and figure 21). Here, it has been further shown that the ϕ_L saturation level stems primarily from the action of the steady drag component. It should be reminded here that the common frequency of vortex shedding, fluid forcing, and cylinder motion increases monotonically with increasing the free-stream velocity due to the non-dispersive nature of the vortices shed in the wake (physical system). As a consequence, both lift frequency and phase remain at a saturation level because a possible increase in f_L^* would entail a corresponding increase in ϕ_L which cannot be accommodated per inequality (5.13). For the saturated response frequency in the lower branch, strong coupling between the cylinder motion and the vortex shedding is still possible (small detuning) so that the response amplitude remains at a high level until the reduced velocity becomes large enough and synchronization is no longer possible (large detuning). The above analysis suggests that lock-in may be absent if the saturation level cannot be reached.

5.4. Upper↔lower transition – the bistable region

5.4.1. Phase dynamics in the bistable region

We have observed a transition region between the upper and lower branches over the range $6.7 < U^* < 7.0$, which we denote as the ‘bistable’ region; it spawns some unique characteristics that are discussed in more detail in this section. Figure 22 presents time series of the instantaneous phase difference between lift and displacement ϕ_L for a sequence of five reduced velocities encompassing the bistable region. The key here is to distinguish the character of fluctuations of the instantaneous ϕ_L in the bistable region from corresponding fluctuations that occur in the neighbouring upper and lower branches. This is facilitated by drawing horizontal lines on the plots marking two different levels at 103° and 122° . At $U^* = 6.6$, i.e. at the end of the upper branch just before the bistable region, ϕ_L displays considerable modulations around the marked lower level. It should be remembered that at this reduced velocity the system is close to the point of unstable equilibrium as discussed in the previous section. Although the instantaneous phase can reach the upper level, the moving average remains considerably below the upper level. In contrast, for reduced velocities in the bistable region, i.e. at $U^* = 6.7, 6.8$, and 6.9 , the moving average phase spends portions of the time on the upper level and some other portions at the lower level. The portion of time spend on the upper level is clearly higher at $U^* = 6.9$ than at $U^* = 6.7$ and 6.8 . Once U^* increases to 7.0 , which corresponds to the start of lower branch just above the bistable region, ϕ_L fluctuates around the upper level only. Thus, the results in figure 22 indicate that for a narrow range of reduced velocities

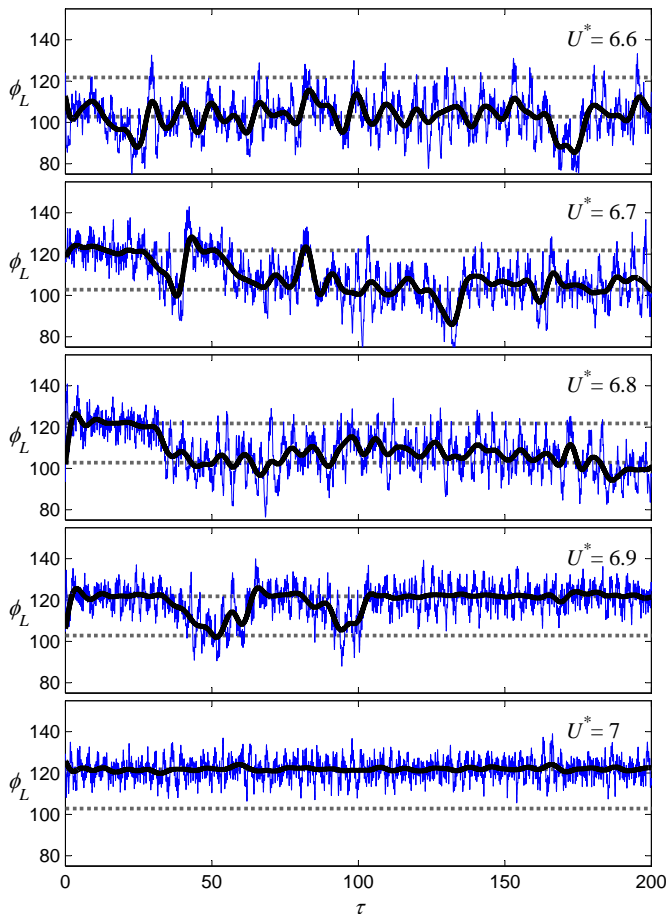


FIGURE 22. (Colour online) Time series of the instantaneous phase between lift and displacement at different reduced velocities encompassing the bistable region. The blue lines denote the instantaneous phase and thick black lines denote the moving average (filtered phase). Values are given in degrees. There is no difference between the wrapped and the unwrapped phases for the cases shown.

two ‘stable equilibria’ co-exist. Each stable equilibrium corresponds to a different value of the phase difference.

Previous studies have shown that such bistable dynamics can result from competition between different modes of vortex shedding in the wake of a cylinder oscillating transversely to a free stream (Morse & Williamson 2009*a,b*; Zhao *et al.* 2014*a*). More specifically, measurements of the vorticity distribution in the wake of cylinders undergoing forced vibration have revealed a region in the map of normalized amplitude and frequency $\{A^* : f^*/U^*\}$ where either the 2S and 2Po, or the 2Po and 2P modes of vortex shedding co-exist (Morse & Williamson 2009*a*). Similar mode competition and switching has also been found in free vibration (Zhao *et al.* 2014*a*). Therefore, the phase dynamics illustrated in this study is most probably affected by intermittent switching between different modes of vortex shedding. In particular, switching between the 2Po and P modes is very likely in the bistable region. Perturbations of or in the system, e.g. cycle-to-cycle variations due to the nature of turbulent flow fluctuations, can cause switching from one stable state to the other. The intermittent switching between the two stable states can be confused with

State	f^*	A^*	C_D	C_L	ϕ_D	ϕ_L
upper branch	0.843	0.658	0.180	1.25	45°	109°
lower branch	0.893	0.544	0.184	1.24	46°	122°

TABLE 3. Properties of the cylinder response and the hydrodynamic force of each state in the bistable region at $U^* = 6.8$.

chaotic oscillations because the phase differences between lift and displacement are not far apart for the two stable states as shown above. However, we consider that this type of intermittent switching in the bistable region is distinct from the chaotic oscillations observed in the second half of the upper branch because each stable state also has different response characteristics as shown in table 3. Interestingly, the magnitude of the drag and lift fluctuations is approximately the same in both stable states.

The two stable states in the bistable region can be further distinguished by looking at the response frequencies of each state, i.e.

$$\begin{aligned} \text{end of upper branch:} & \quad f^* = 1.160 \Leftrightarrow f = 0.997f_n, \\ \text{start of lower branch:} & \quad f^* = 1.249 \Leftrightarrow f = 1.073f_n. \end{aligned}$$

It should be noted that f^* is the response frequency normalized by the natural frequency determined from free decay tests in still water ($f_{n,\text{water}}$) while we take the natural frequency of the system (f_n) to be the one in vacuum, which can be approximated by the value determined from free decay tests in still air ($f_{n,\text{air}}$), i.e.

$$\frac{f}{f_n} \approx \frac{f_{n,\text{water}}}{f_{n,\text{air}}} \frac{f}{f_{n,\text{water}}} = 0.859f^*. \quad (5.14)$$

Thus, the response frequency is lower than the natural frequency of the hydro-elastic cylinder in the upper branch whereas it is higher in the lower branch. The above observation might indicate that phase switching in the bistable region is also related to the dynamics posed by the equation of cylinder free motion.

5.4.2. The phase jump at upper↔lower transition

The upper↔lower transition involves a jump in both the response amplitude and frequency as well as in the phase difference between lift and displacement. The origin of these jumps can be analysed with the aid of the hydrodynamic model of drag and lift components and the equation of cylinder free motion. Now, the component of the transverse force in-phase with displacement can be obtained from the equation of cylinder motion, assuming sinusoidal oscillation, which yields

$$C_y \cos \phi = 2\pi^3(m^* + 1) \frac{A^*}{U^{*2}} \left[1 - \left(\frac{f}{f_n} \right)^2 \right], \quad (5.15)$$

where the reduced velocity U^* is normalized using the natural frequency determined from free-decay tests in still water ($f_{n,\text{water}}$) in keeping with the presentation of the results. It follows directly from equation (5.15) that

$$C_y \cos \phi \geq 0 \quad \text{or} \quad -90^\circ < \phi \leq 90^\circ \quad \text{if} \quad f \leq f_n, \quad (5.16)$$

$$C_y \cos \phi < 0 \quad \text{or} \quad 90^\circ < \phi \leq 270^\circ \quad \text{if} \quad f > f_n. \quad (5.17)$$

From equations (5.3) and (5.4) of the hydrodynamical model, the component of the transverse force in phase with the cylinder displacement can be written as

$$C_y \cos \phi = C_L \cos \phi_L - \frac{\pi f^* A^*}{U^*} C_D \cos \phi_D. \quad (5.18)$$

Thus, according to (5.16) and (5.17) once the oscillation frequency passes through the crossover point where $f = f_n$, the term $C_y \cos \phi$ must change sign. In the second half of the upper branch, before the crossover point where $f \leq f_n$, the requirement $C_y \cos \phi \geq 0$ from (5.16) cannot be satisfied because $\phi_L > 90^\circ$ and both terms on the right-hand side of (5.18) are negative. As discussed in the previous section, in the second half of the upper branch the hydrodynamics are incompatible with the equation of cylinder free motion (see also figure 21). However, as long as $f > f_n$ ϕ_L can take values above 90° without violating the restrictions posed by the equation of cylinder free motion in (5.17). This is consistent with measured values in the lower branch where $\phi_L \approx 122^\circ$.

In order to verify the above arguments, we present the variation of $C_y \cos \phi$ as a function of U^* in figure 23. The first method to determine $C_y \cos \phi$ is from measurements of A^* and f^* and the equation of cylinder motion (5.15), which can be rewritten as

$$C_y \cos \phi = 2\pi^3 m^* \frac{A^*}{U^{*2}} \left[\left(\frac{f_{n,\text{air}}}{f_{n,\text{water}}} \right)^2 - f^{*2} \right]. \quad (5.19)$$

This method assumes that the motion is pure harmonic. The second method is from direct measurements of C_y and ϕ , which are presented in §4.1. The third method is using equation (5.18) and indirect measurements of C_L , C_D , ϕ_L , and ϕ_D , which are presented in §4.2. Generally, the methods based on direct and indirect measurements agree satisfactorily over the entire range of reduced velocities with some minor deviations. This provides a self-consistency check that the data processing methods employed for obtaining the drag and lift components do not introduce considerable inaccuracies. Both direct and indirect measurements agree well with values obtained from the equation of cylinder motion in the initial branch and in the first half of the upper branch. As expected from the equation of cylinder motion $C_y \cos \phi$ first becomes negative at $U^* \geq 6.7$, which corresponds to the point where f (time-averaged value) exceeds the natural frequency of the system, $f > f_n$. In contrast, both direct and indirect measurements show that $C_y \cos \phi$ becomes negative earlier in the middle of the upper branch ($U^* \geq 6.0$). It may be further noted that the difference between results from force measurements and from the equation of cylinder motion is most marked around the crossover point ($U^* = 6.6$) but considerable deviations can also be observed in the lower branch ($U^* \geq 7$). Such deviations may be attributable to deviations of the cylinder response from the ideal harmonic motion.

According to the above analysis, the jump in ϕ_L in tandem with simultaneous jumps in A^* and f^* can be linked to the elimination of the restriction $\phi_L < 90^\circ$ posed by the equation of cylinder motion for vibration frequencies $f \leq f_n$. Once the vibration frequency exceeds $f > f_n$, ϕ_L jumps at the preferred value that simultaneously satisfies both the hydrodynamics of the unsteady wake and the dynamics of the cylinder free motion.

6. Conclusions

In this study, we employed a decomposition of the total hydrodynamic force acting on a circular cylinder undergoing transverse VIV into effective drag and lift components in order to analyse the dynamical response for a hydro-elastic cylinder with a mass

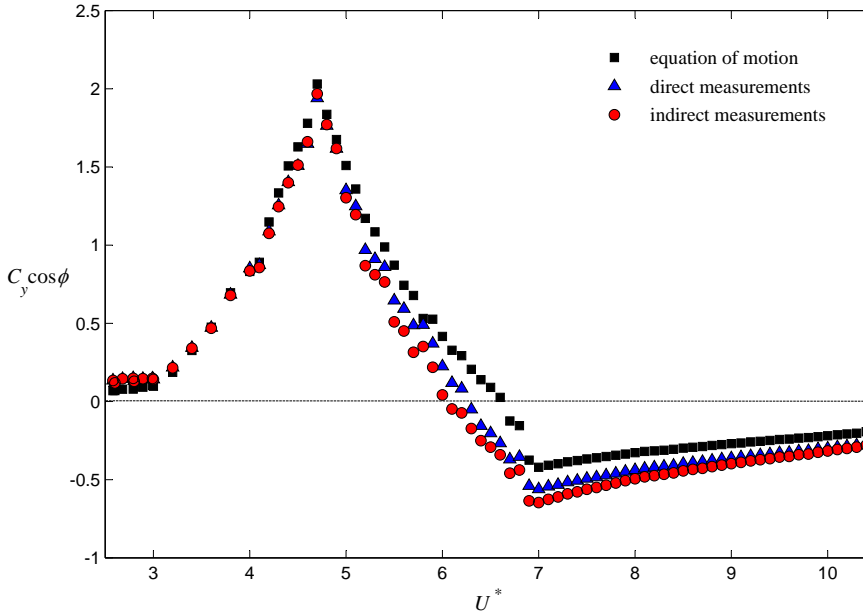


FIGURE 23. (Colour online) Variation of the force component in-phase with displacement, $C_y \cos \phi$, as a function of the reduced velocity, U^* , as determined by the equation of cylinder motion, direct and indirect measurements (see the text).

ratio of 3.00 and damping ratio of 0.0035. We considered the hydro-elastic cylinder as a non-linear dynamical system and examined the phase dynamics of the fluid forcing in the synchronization range. For this purpose, we computed the instantaneous phase difference between fluid forcing and cylinder displacement or relative velocity using the Hilbert transform. Time series of both the wrapped phase and the unwrapped phase have been presented in order to fully characterize the dynamics.

The hydro-elastic cylinder has very low values of mass and structural damping for which three distinct regions of significant response are observed, i.e. the initial, upper, and lower branches. In the second half of the upper branch, the time series of the wrapped phase exhibits sudden jumps that are difficult to interpret. Within the latter range, the unwrapped phase difference between the transverse force and displacement ϕ either *a*) displays periods of constant value separated by phase slips or *b*) becomes unbounded, i.e. ϕ drifts continuously. This highly irregular phase dynamics indicates a phenomenological loss of phase locking, paradoxically in the middle of the synchronization range. This finding is consistent with the discovery of chaotic vibrations near the middle of the upper branch by Zhao *et al.* (2014a). In contrast, the phase difference between lift and displacement ϕ_L remains stable, which illustrates that the unsteady wake flow and the cylinder motion are synchronized throughout the upper branch. We maintain that this relationship becomes clear because lift fluctuations are intrinsically linked with the vortex dynamics in the wake of the vibrating cylinder. The instantaneous ϕ_L displays comparatively significant modulations in the second half of the upper branch, which is probably the cause of phenomenologically chaotic phase dynamics of the transverse force.

An important finding of the present study is that the mean phase lag between lift and cylinder displacement varies linearly with the vibration frequency, which is consistent with the dynamics of physical systems where frequency and phase are intrinsically related. The new approach used in the present study avoids the ambiguity in the measurements of

the phase difference between the transverse force and displacement ϕ which, for systems with very low damping ratio, is restricted to extremely narrow ranges of permissible values just above 0° or just below 180° throughout the synchronization range. In contrast to the restricted ϕ values, the phase difference between the lift and displacement ϕ_L increases in the upper branch, whereas ϕ_L remains nearly constant in the lower branch, which highlights the different dynamics in these two branches.

The results show that the drag induces a component which always opposes the cylinder velocity, i.e. it acts as a source of damping, whereas the lift component induces a component which drives the cylinder motion, in agreement with purely theoretical considerations. A key finding is that the magnitude of the unsteady lift C_L varies linearly with the kinematical parameter f^*A^*/U^{*2} , which is the scaling of the traditional excitation coefficient in-phase with cylinder velocity $C_y \sin \phi$ expected from the equation of cylinder free motion.

An analytical model is introduced for the unsteady lift and the steady and unsteady drag components, which explains well the observed dynamics. In the middle of the upper branch, the hydro-elastic cylinder reaches a point of unstable equilibrium where the system is most sensitive to small perturbations. When increasing the reduced velocity in the second half of the upper branch, there exist competing requirements resulting from (i) the hydrodynamics of the unsteady wake, which dictates that the lift phase with respect to displacement has to increase as the oscillation frequency increases, and (ii) the dynamics of cylinder free motion, which, assuming that the motion is pure harmonic, limits the permissible range of the lift phase to remain fixed at approximately 90° . The competing requirements are balanced in practice by deviations of the cylinder motion from the ideal pure harmonic.

For a narrow range of reduced velocity over the transition between the upper and lower branches, bistable dynamics emerge where two stable states exist over different portions of time. Each state is characterized by different response amplitude, frequency, and lift phase. The two states are most probably associated with the 2Po and 2P modes of vortex formation found in the wake of oscillating cylinders (Morse & Williamson 2009a; Zhao *et al.* 2014a). The bistable region has distinct features from the region of chaotic vibrations at the second half of the upper branch.

As a corollary, the force decomposition adopted in this study provides a theoretical framework for better understanding the dynamics of VIV of a rigid circular cylinder with a single degree of freedom to oscillate in the transverse direction. It would be of interest to extend this force decomposition method in the future to analyse the dynamics of the less-well understood case of a hydro-elastic cylinder with two degrees of freedom in both streamwise and transverse directions. Furthermore, the analytical model may be incorporated in refined semi-empirical codes for predicting VIV of long flexible cylinders.

REFERENCES

- BEARMAN, P. W. 1984 Vortex shedding from oscillating bluff bodies. *Annual Review of Fluid Mechanics* **16** (1), 195–222.
- BEARMAN, P. W. 2009 Understanding and predicting vortex-induced vibrations. *Journal of Fluid Mechanics* **634**, 1–4.
- BEARMAN, P. W. 2011 Circular cylinder wakes and vortex-induced vibrations. *Journal of Fluids and Structures* **27** (5), 648 – 658.
- BLEVINS, R. D. 2001 *Flow-induced vibration*. Florida: Krieger Publishing Company.
- BLEVINS, R. D. 2009 Models for vortex-induced vibration of cylinders based on measured forces. *Journal of Fluids Engineering, Transactions ASME* **131** (10), 1–9, 101203.
- BLEVINS, R. D. & COUGHRAN, C. S. 2009 Experimental investigation of vortex-induced

- vibration in one and two dimensions with variable mass, damping, and Reynolds number. *Journal of Fluids Engineering, Transactions ASME* **131** (10), 1–7, 101202.
- BRANKOVIĆ, M. & BEARMAN, P. W. 2006 Measurements of transverse forces on circular cylinders undergoing vortex-induced vibration. *Journal of Fluids and Structures* **22**, 829–836.
- CARBERRY, J., SHERIDAN, J. & ROCKWELL, D. 2005 Controlled oscillations of a cylinder: forces and wake modes. *Journal of Fluid Mechanics* **538**, 31–69.
- COHEN, L. 1995 *Time-frequency analysis*. New Jersey: Prentice Hall PTR.
- FENG, C. C. 1968 The measurement of vortex induced effects in flow past stationary and oscillating circular and D-section cylinders. Master's thesis, The University of British Columbia.
- GABBAI, R. D. & BENAROYA, H. 2005 An overview of modeling and experiments of vortex-induced vibration of circular cylinders. *Journal of Sound and Vibration* **282** (3), 575 – 616.
- GHARIB, M. Z. 1999 Vortex-induced vibration, absence of lock-in and fluid force deduction. Phd thesis, California Institute of Technology.
- GOPALKRISHNAN, R. 1993 Vortex-induced forces on oscillating bluff cylinders. Phd thesis, Massachusetts Institute of Technology.
- GOVARDHAN, R. & WILLIAMSON, C. H. K. 2000 Modes of vortex formation and frequency response of a freely vibrating cylinder. *Journal of Fluid Mechanics* **420**, 85–130.
- GRIFFIN, O. M. 1981 OTEC cold water pipe design for problems caused by vortex-excited oscillations. *Ocean Engineering* **8** (2), 129–209.
- HOVER, F. S., TECHET, A. H. & TRIANTAFYLLOU, M. S. 1998 Forces on oscillating uniform and tapered cylinders in crossflow. *Journal of Fluid Mechanics* **363**, 97–114.
- KHALAK, A. & WILLIAMSON, C. H. K. 1996 Dynamics of a hydroelastic cylinder with very low mass and damping. *Journal of Fluids and Structures* **10** (5), 455–472.
- KHALAK, A. & WILLIAMSON, C. H. K. 1997 Fluid forces and dynamics of a hydroelastic structure with very low mass and damping. *Journal of Fluids and Structures* **11** (8), 973 – 982.
- KHALAK, A. & WILLIAMSON, C. H. K. 1999 Motions, forces and mode transitions in vortex-induced vibrations at low mass-damping. *Journal of Fluids and Structures* **13** (7-8), 813–851.
- KING, R. 1977 A review of vortex shedding research and its application. *Ocean Engineering* **4** (3), 141 – 171.
- KLAMO, J. T., LEONARD, A. & ROSHKO, A. 2006 The effects of damping on the amplitude and frequency response of a freely vibrating cylinder in cross-flow. *Journal of Fluids and Structures* **22** (6-7), 845–856.
- KONSTANTINIDIS, E. 2013 Apparent and effective drag for circular cylinders oscillating transverse to a free stream. *Journal of Fluids and Structures* **39**, 418 – 426.
- KONSTANTINIDIS, E. 2014 On the response and wake modes of a cylinder undergoing streamwise vortex-induced vibration. *Journal of Fluids and Structures* **45**, 256 – 262.
- KONSTANTINIDIS, E. 2017 Comment on lock-in in forced vibration of a circular cylinder [phys. fluids 28, 113605 (2016)]. *Physics of Fluids* **29** (10), 109101.
- KONSTANTINIDIS, E. & BOURIS, D. 2016 Vortex synchronization in the cylinder wake due to harmonic and non-harmonic perturbations. *Journal of Fluid Mechanics* **804**, 248277.
- KONSTANTINIDIS, E. & LIANG, C. 2011 Dynamic response of a turbulent cylinder wake to sinusoidal inflow perturbations across the vortex lock-on range. *Physics of Fluids* **23** (7), 075102.
- LEE, J.H. & BERNITSAS, M.M. 2011 High-damping, high-reynolds viv tests for energy harnessing using the vivace converter. *Ocean Engineering* **38** (16), 1697 – 1712.
- LEONTINI, J.S., THOMPSON, M.C. & HOURIGAN, K. 2006a The beginning of branching behaviour of vortex-induced vibration during two-dimensional flow. *Journal of Fluids and Structures* **22** (6), 857 – 864.
- LEONTINI, J. S., STEWART, B. E., THOMPSON, M. C. & HOURIGAN, K. 2006b Wake state and energy transitions of an oscillating cylinder at low reynolds number. *Physics of Fluids* **18** (6), 067101.

- LUCOR, D., FOO, J. & KARNIADAKIS, G. E. 2005 Vortex mode selection of a rigid cylinder subject to VIV at low mass-damping. *Journal of Fluids and Structures* **20**, 483–503.
- MARZOUK, O. A. 2011 One-way and two-way couplings of cfd and structural models and application to the wake-body interaction. *Applied Mathematical Modelling* **35** (3), 1036 – 1053.
- MORSE, T. L. & WILLIAMSON, C. H. K. 2009a Fluid forcing, wake modes, and transitions for a cylinder undergoing controlled oscillations. *Journal of Fluids and Structures* **25**, 697–712.
- MORSE, T. L. & WILLIAMSON, C. H. K. 2009b Prediction of vortex-induced vibration response by employing controlled motion. *Journal of Fluid Mechanics* **634**, 5–39.
- MORSE, T. L. & WILLIAMSON, C. H. K. 2010 Steady, unsteady and transient vortex-induced vibration predicted using controlled motion data. *Journal of Fluid Mechanics* **649**, 429451.
- NEMES, A., ZHAO, J., LO JACONO, D. & SHERIDAN, J. 2012 The interaction between flow-induced vibration mechanisms of a square cylinder with varying angles of attack. *Journal of Fluid Mechanics* **710**, 102130.
- PARKINSON, G. V. 1971 Wind-induced instability of structures. *Philosophical Transactions of the Royal Society of London. Series A, Mathematical and Physical Sciences* **269** (1199), 395–413.
- PIKOVSKY, A., ROSENBLUM, M., KURTHS, J. & STROGATZ, S. 2001 *Synchronization: A Universal Concept in Nonlinear Sciences*. Cambridge University Press.
- SARPKAYA, T. 2004 A critical review of the intrinsic nature nature of vortex-induced vibrations. *Journal of Fluids and Structures* **19**, 389–447.
- SOTI, A. K., ZHAO, J., THOMPSON, M. C., SHERIDAN, J. & BHARDWAJ, R. 2018 Damping effects on vortex-induced vibration of a circular cylinder and implications for power extraction. *Journal of Fluids and Structures* **81**, 289 – 308.
- TANIDA, Y., OKAJIMA, A. & WATANABE, Y. 1973 Stability of a circular cylinder oscillating in uniform flow or in a wake. *Journal of Fluid Mechanics* **61** (4), 769784.
- WILLIAMSON, C. H. K. & GOVARDHAN, R. 2004 Vortex-induced vibrations. *Annual Review of Fluid Mechanics* **36**, 413–455.
- ZHAO, J., LEONTINI, J.S., LO JACONO, D. & SHERIDAN, J. 2014a Chaotic vortex induced vibrations. *Physics of Fluids* **26** (12), 121702.
- ZHAO, J., LEONTINI, J.S., LO JACONO, D. & SHERIDAN, J. 2014b Fluidstructure interaction of a square cylinder at different angles of attack. *Journal of Fluid Mechanics* **747**, 688721.